







Detection of Ghost Targets for Automotive Radar in the Presence of Multipath

Le Zheng , Senior Member, IEEE, Jiamin Long , Marco Lops , Fellow IEEE, Fan Liu , Senior Member, IEEE, Xueyao Hu , and Chuanhao Zhao 

Abstract—Colocated multiple-input multiple-output (MIMO) technology has been widely used in automotive radars as it provides accurate angular estimation of the objects with a relatively small number of transmitting and receiving antennas. Since the Direction Of Departure (DOD) and the Direction Of Arrival (DOA) of *line-of-sight* targets coincide, MIMO signal processing allows for the formation of a larger virtual array for angle finding. However, multiple paths impinging the receiver is a major limiting factor, in that radar signals may bounce off obstacles, creating echoes for which the DOD does not equal the DOA. Thus, in complex scenarios with multiple scatterers, the direct paths of the intended targets may be corrupted by indirect paths from other objects, which leads to inaccurate angle estimation or ghost targets. In this paper, we focus on detecting the presence of ghosts due to multipath by regarding it as the problem of deciding between a *composite* hypothesis, \mathcal{H}_0 say, that the observations only contain an unknown number of direct paths sharing the same (unknown) DOD's and DOA's, and a *composite* alternative, \mathcal{H}_1 say, that the observations also contain an unknown number of indirect paths, for which DOD's and DOA's do not coincide. We exploit the Generalized Likelihood Ratio Test (GLRT) philosophy to determine the detector structure, offering closed-form expressions for theoretical detection performance, and a convex waveform optimization approach to improve detection performance. In practical scenarios, the

unknown parameters of GLRT philosophy are replaced by carefully designed estimators. The angles of both the active direct paths and of the multi-paths are indeed estimated through a sparsity-enforced Compressed Sensing (CS) approach with Levenberg-Marquardt (LM) optimization to estimate the angular parameters in the continuous domain. Simulation and experimental results are finally offered in order to validate the proposed solution.

Index Terms—Automotive radar, Colocated multiple-input multiple-output (MIMO), multipath, GLRT, group sparse.

I. INTRODUCTION

IN recent years, the need for safer driving has led to a significant demand for automotive radar [1], [2], [3], [4]. Colocated multiple-input multiple-output (MIMO) technology has been proven to be effective in providing accurate angular estimation of objects with a relatively small number of antennas, making it popular in the automotive industry [5], [6], [7].

One major challenge of colocated MIMO systems is the multipath reflection, where the target's echo takes multiple paths to reach the receiver, including direct and indirect paths [8], [9], [10], [11]. Direct paths involve the signal being transmitted from the radar to the target and then reflected back to the radar directly, while the indirect paths could bounce multiple times between reflectors. Usually, due to different propagation delays, range gating can get rid of the indirect paths from the target we are trying to detect. However, the direction of departure (DOD) of the signal does not equal the direction of arrival (DOA) for some indirect paths, [5], [12], so the assumption of colocated MIMO does not hold. As a consequence, in multi-target scenarios, the direct paths of intended targets may be corrupted by indirect paths from other objects, and applying classical angle finding algorithms may result in degraded angle estimation accuracy and detection of ghost targets.

To detect ghost targets, some researchers exploit the geometrical relationships of the detections in the delay-Doppler domain. Specifically, R. Feng et al. employed the Hough transform to explore the linear relationship of the multipath detections [13]. F. Ross et al. detected the ghost targets by analyzing the Doppler distribution of moving targets [14]. These methods can be effective when the speed of the ghost target is significant, and the efficient utilization of Doppler information can aid in extracting geometric information from multipaths for identification. Notably, the authors in [15] proposed a novel method to suppress ghosts through waveform design, which effectively

Manuscript received 19 September 2023; revised 3 February 2024 and 21 March 2024; accepted 24 March 2024. Date of publication 4 April 2024; date of current version 2 May 2024. This work was supported in part by the National Natural Science Foundation of China under Grant 62388102. The work of Marco Lops was supported in part by the European Union under the Italian National Recovery and Resilience Plan (PNRR) of NextGenerationEU, partnership on “Telecommunications of the Future” (PE00000001—program “RESTART”—E63C22002040007) and in part by the Project PRIN-2022 under Grant #E53D23000410006. The associate editor coordinating the review of this manuscript and approving it for publication was Prof. Wei Yi. (Corresponding author: Xueyao Hu.)

Le Zheng, Jiamin Long, and Chuanhao Zhao are with the School of Information and Electronics, Beijing Institute of Technology, Beijing 100081, China, and also with Chongqing Innovation Center, Beijing Institute of Technology, Chongqing 401120, China (e-mail: le.zheng.cn@gmail.com; jiaminlong0548@163.com; 13041258366@163.com).

Marco Lops is with the Department of Electrical and Information Technology (DIETI), University of Naples Federico II, 80138 Naples, Italy, and also with the Consorzio Nazionale Interuniversitario per le Telecomunicazioni, 43124 Parma, Italy (e-mail: lops@unina.it).

Fan Liu is with the Department of Electronic and Electrical Engineering, Southern University of Science and Technology, Shenzhen 518055, China (e-mail: liuf6@sustech.edu.cn).

Xueyao Hu is with the School of Information and Electronics, Beijing Institute of Technology, Beijing 100081, China, also with the Chongqing Innovation Center, Beijing Institute of Technology, Chongqing 401120, China, and also with the Electromagnetic Sensing Research Center of CEMEE State Key Laboratory, Beijing 100081, China (e-mail: xueyao.hu@qq.com).

Digital Object Identifier 10.1109/TSP.2024.3384750

controls the responses of distinct delay-Doppler cells with a high degree of precision. However, in situations with densely distributed objects, ghost targets with low speeds may couple with the stationary objects, making it difficult to use Doppler information to identify them.

Several strategies for multipath ghost suppression in the angular domain have been proposed so far, ranging from antenna design [9], [16] to synthetic aperture radar (SAR) [17] and deep learning [18]. Alternative deep neural network (DNN) [19] method seeks to verify DOD and DOA equality but may overlook complexities from mixed paths within a delay-Doppler cell. Considering the potential advantages of indirect paths in non-line-of-sight detection [20], [21] or reconfigurable intelligent surface (RIS) applications [22], accurately detecting and estimating the parameters of each path is more valuable than simply suppressing multipath: this is the idea underlying [23], where the presence of multipath reflections is detected through a Generalized Likelihood Ratio Test (GLRT). The detector was developed under a specific signal model where only two TX antennas are used and all indirect paths for a target are confined to a single delay-Doppler cell. However, in automotive radars, MIMO arrays typically incorporate more TX antennas [24] and a single delay-Doppler cell can contain paths from multiple targets. Given the potential model mismatch, the performance of angle estimation in [23] degrades in such situations and the GLRT would fail.

Accurate estimation of target information is crucial for ghost detection in the angular domain, particularly in scenarios involving mixed first-order and direct paths. The coexistence of these paths often results in significant mutual interference, while discrepancies in DOD and DOA for indirect paths further complicate estimations, posing a challenge to achieving high accuracy angle measurements. In the field of bistatic MIMO radar, the angle finding methods for situations with different DOA and DOD have been widely studied. Subspace methods, such as the two-dimensional multiple signal classification (2D-MUSIC) [25] and unitary-estimation of signal parameters via rotational invariance technique (U-ESPRIT) [26] have been proposed. These methods have limitations related to signal and noise characteristics, array geometry, and computational complexity, which make them unsuitable for automotive radars. In [27], minimum variance distortionless response (MVDR) is utilized for spectrum estimation, addressing grating lobes in sparse MIMO radar by proposing a suppression method tailored for multipath environments. In [28], an iterative adaptive approach (IAA) was employed to estimate the two-dimensional spatial spectrum for automotive radar, while in [29], the authors propose a joint direction of departure (DOD) and direction of arrival (DOA) estimation method by comparing the power distribution of the IAA spectrum. More recent techniques based on compressed sensing (CS) theory [30] provide an alternative for jointly estimating the DOD and DOA [31], [32]. The performance of these methods depends on the designed dictionaries and gridding scheme in the angular domain. However, as the paths are usually specified by parameters in a continuous domain, the discretization usually leads to model mismatch and degradation in estimation [33], [34].

In this paper, we further investigate ghost target detection in the angular domain, to the end of detecting the indirect paths and allowing their removal, so as to preserve only the direct paths from the target. Two types of paths are considered in our analysis: direct paths, exhibiting the same DOD and DOA, and first-order paths (more on this in Section II) whose DOD does not equal DOA. After deriving the MIMO radar signal model, the problem of first-order paths existence is stated as a binary decision problem between a composite hypothesis, \mathcal{H}_0 say, that the observations only contain an unknown number of direct paths sharing the same (unknown) DOD's and DOA's, and a *composite* alternative, \mathcal{H}_1 say, that the observations also contain an unknown number of indirect paths, for which DOD's and DOA's do not coincide. In this context, we resort to the GLRT philosophy to determine the detector structure and propose a convex waveform optimization approach to enhance detection performance. As for the implementable solution, the unknown parameters of GLRT philosophy are replaced by carefully designed estimators. In particular, to estimate the angle of the paths under the two alternative hypotheses, we develop CS methods in the continuous domain for the cases with and without first-order paths, respectively. Specifically, in the situation with first-order paths, the algorithm is designed with a group-sparsity enforced structure to take advantage of the reversibility of the propagation path. To improve the convergence performance, we adopt a Levenberg-Marquardt (LM) optimization approach to accelerate the execution of the algorithm. The proposed method has shown superior performance over existing methods by simulation. An extensive performance assessment is finally offered in order to validate the proposed strategy.

The remainder of the paper is organized as follows: In Section II, we present the signal model of multipath reflection. Section III details the proposed detector and derives its exact theoretical performance. In Section IV, we describe the proposed angle estimation methods under different situations. In Section V, we present the simulation results, and finally, Section VI concludes the paper.

Notation : The transposition, Hermitian transposition, inversion, pseudo-inversion, Kronecker product, Khatri-Rao (KR) product, Hadamard product and direct sum operations are denoted by $(\cdot)^T$, $(\cdot)^H$, $(\cdot)^{-1}$, $(\cdot)^\dagger$, \otimes , \circ , \odot , \oplus , respectively. Matrix \mathbf{X} and vector \mathbf{x} are indicated in boldface. The notation $\text{diag}(\mathbf{X})$ denotes the operation of extracting elements from the diagonal of \mathbf{X} to form a new vector. $\|\mathbf{x}\|_2 = \sqrt{\sum_i x_i^2}$ denotes the ℓ_2 -norm. $\mathcal{R}(\mathbf{X})$ denote the range-span of the matrix \mathbf{X} . $\mathbf{x}^{(k)}$ denotes the value of \mathbf{x} at the k -th iteration and $\mathbf{x}^{(k,j)}$ denotes the value of $\mathbf{x}^{(k)}$ at the j -th iteration. \mathbf{I}_n being the $n \times n$ identity matrix. For \mathbf{X} , the n -th column vector and (m, n) -th element are denoted by $\mathbf{X}(n)$ and $[\mathbf{X}]_{m,n}$, respectively, while the m -th element of vector \mathbf{x} is given by $[\mathbf{x}]_m$.

II. SIGNAL MODEL AND PROBLEM FORMULATION

State-of-the-art automotive radars usually employ Frequency Modulated Continuous Wave (FMCW) sequences to enable high-resolution estimation of target range and radial velocity [35], [36], and adopt colocated MIMO technology to synthesize

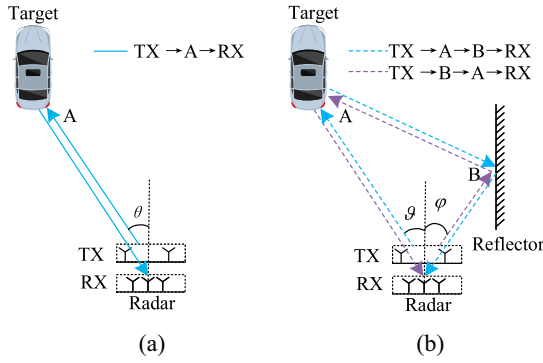


Fig. 1. (a) A direct path, (b) a pair of first-order paths.

a large virtual array for accurate angle estimation using multiple transmit and receive antennas. We consider a colocated MIMO radar system with M_T transmit antennas emitting as many coded sequences [37] and M_R receive antennas. At the receiver end, the signal at each antenna undergoes the usual processing to extract the contribution of each transmit antenna and synthesize a MIMO channel with $M_T M_R$ elements. This signal is then processed via fast Fourier transform (FFT) along fast and slow time to obtain the delay-Doppler profile of the echo path [1]. Finally, the virtual array response of the detected target can be constructed to estimate the direction of targets [6].

The multipath scenario can be visualized as a radar emitting signals that bounce off a target and a reflector. As depicted in Fig. 1, where the target is placed at position A and the reflector is located at point B, the signals received by the radar can take different paths as follows:

- *Direct path*: The shortest path between the radar and the target, where the departure and arrival angles of the direct path are equal to the target angle as shown in Fig. 1(a).
- *First-order paths*: The indirect paths involve a single bounce at the reflector on the way of departure or arrival, resulting in a longer delay compared to the direct path. As shown in Fig. 1(b), the DOD's of the first-order paths do not equal the respective DOA's.
- *Higher-order paths*: The indirect paths involve more bounces before the echo reaches the receiver. However, due to the attenuation caused by scattering at the target and reflectors, higher-order paths are normally weak, and may thus be neglected [13], [38].

In automotive radar, delay and Doppler information of direct path yields target range and velocity [2], respectively. Both DOD and DOA equal the angle of far-field targets, enabling the virtual array to form an aperture larger than the physical aperture of the radar, thereby enhancing angular resolution and accuracy of angle estimation [5], [24], [39]. Although Fig. 1 depicts, for simplicity reasons, a single target scenario, the situation we consider here is one wherein multiple reflecting objects are present in the radar field of view, whereby the direct paths generated by the intended targets may end up being corrupted by the first-order paths generated by other reflecting objects.

Consider a FMCW MIMO radar that transmits L pulses from each transmit antenna and exploits slow-time coding as a multiplexing approach. Denote $\mathbf{x}(l) = [x_1(l), x_2(l), \dots, x_{M_T}(l)]^T$

as the vector of the code transmitted at the l -th epoch by the M_T transmit antennas, the transmitted code matrix can be represented as $\mathbf{X} = [\mathbf{x}(1), \mathbf{x}(2), \dots, \mathbf{x}(L)] \in \mathbb{C}^{M_T \times L}$. After performing FFT on the fast-time of received measurements, we consider K_0 direct paths and K_1 pairs of first-order paths in a given delay cell under test and model the observation $\mathbf{y}(l) \in \mathbb{C}^{M_R \times 1}$ as

$$\begin{aligned} \mathbf{y}(l) = & \sum_{k=1}^{K_0} \alpha_k e^{j2\pi f_d(l-1)} \mathbf{a}_R(\theta_k) \mathbf{a}_T^T(\theta_k) \mathbf{x}(l) \\ & + \sum_{k=1}^{K_1} \beta_{k,1} e^{j2\pi f_d(l-1)} \mathbf{a}_R(\varphi_k) \mathbf{a}_T^T(\vartheta_k) \mathbf{x}(l) \\ & + \sum_{k=1}^{K_1} \beta_{k,2} e^{j2\pi f_d(l-1)} \mathbf{a}_R(\vartheta_k) \mathbf{a}_T^T(\varphi_k) \mathbf{x}(l) + \mathbf{w}(l), \quad (1) \end{aligned}$$

where

- α_k , $\beta_{k,1}$ and $\beta_{k,2}$ represent the complex amplitude of the k -th direct path for $k = 1, 2, \dots, K_0$ and the k -th pair first-order paths for $k = 1, 2, \dots, K_1$ respectively. The amplitudes depend on a number of factors such as the transmit power, antenna gain pattern, path loss propagation, reflection coefficient, and matched-filter gain.
- θ_k denotes the DOD of the k -th direct path, which is equal to the DOA; ϑ_k and φ_k denote the DOD and DOA of the k -th pair first-order path with $\vartheta_k \neq \varphi_k$; f_d is the normalized Doppler frequency.
- $\mathbf{a}_T(\cdot) \in \mathbb{C}^{M_T \times 1}$ and $\mathbf{a}_R(\cdot) \in \mathbb{C}^{M_R \times 1}$ are the steering vectors

$$\mathbf{a}_T(\theta) = \frac{1}{\sqrt{M_T}} \begin{bmatrix} e^{j2\pi d_{T,1} \sin(\theta)/\lambda}, e^{j2\pi d_{T,2} \sin(\theta)/\lambda}, \dots, \\ e^{j2\pi d_{T,M_T} \sin(\theta)/\lambda} \end{bmatrix}^T, \quad (2)$$

$$\mathbf{a}_R(\phi) = \frac{1}{\sqrt{M_R}} \begin{bmatrix} e^{j2\pi d_{R,1} \sin(\phi)/\lambda}, e^{j2\pi d_{R,2} \sin(\phi)/\lambda}, \dots, \\ e^{j2\pi d_{R,M_R} \sin(\phi)/\lambda} \end{bmatrix}^T, \quad (3)$$

with θ and ϕ denoting the angles of $\mathbf{a}_T(\cdot)$ and $\mathbf{a}_R(\cdot)$, respectively, λ denoting the wavelength, $d_{T,m}$ and $d_{R,n}$ denoting the relative distances of the m -th TX element and the n -th RX element from the reference array element.

- $\mathbf{w}(l) \in \mathbb{C}^{M_R \times 1}$ is the white Gaussian noise at the radar receive array, distributed as $\mathcal{CN}(\mathbf{0}, \sigma^2 \mathbf{I}_{M_R})$, with σ^2 denoting the noise variance [40].

Denoting $\mathbf{P}(f_d) = \text{diag}([1, e^{j2\pi f_d}, \dots, e^{j2\pi f_d(L-1)}])$, the received data matrix reads

$$\begin{aligned} \mathbf{Y} = & [\mathbf{y}(1), \mathbf{y}(2), \dots, \mathbf{y}(L)] \\ = & \sum_{k=1}^{K_0} \alpha_k \mathbf{a}_R(\theta_k) \mathbf{a}_T^T(\theta_k) \mathbf{X} \mathbf{P}(f_d) \\ & + \sum_{k=1}^{K_1} \beta_{k,1} \mathbf{a}_R(\varphi_k) \mathbf{a}_T^T(\vartheta_k) \mathbf{X} \mathbf{P}(f_d) \\ & + \sum_{k=1}^{K_1} \beta_{k,2} \mathbf{a}_R(\vartheta_k) \mathbf{a}_T^T(\varphi_k) \mathbf{X} \mathbf{P}(f_d) + \mathbf{W}, \quad (4) \end{aligned}$$

where $\mathbf{W} = [\mathbf{w}(1), \mathbf{w}(2), \dots, \mathbf{w}(L)]$. Plain matched filtering thus yields

$$\begin{aligned} \mathbf{Z} &= \mathbf{Y}(\mathbf{X}\mathbf{P}(f_d))^H \\ &= \sum_{k=1}^{K_0} \alpha_k \mathbf{a}_R(\theta_k) \mathbf{a}_T^T(\theta_k) \mathbf{X}\mathbf{P}(f_d) \mathbf{P}^H(f_d) \mathbf{X}^H \\ &\quad + \sum_{k=1}^{K_1} \beta_{k,1} \mathbf{a}_R(\varphi_k) \mathbf{a}_T^T(\vartheta_k) \mathbf{X}\mathbf{P}(f_d) \mathbf{P}^H(f_d) \mathbf{X}^H \\ &\quad + \sum_{k=1}^{K_1} \beta_{k,2} \mathbf{a}_R(\vartheta_k) \mathbf{a}_T^T(\varphi_k) \mathbf{X}\mathbf{P}(f_d) \mathbf{P}^H(f_d) \mathbf{X}^H \\ &\quad + \mathbf{W}\mathbf{P}^H(f_d) \mathbf{X}^H, \end{aligned} \quad (5)$$

where $\mathbf{P}(f_d) \mathbf{P}^H(f_d) = \mathbf{I}_L$. Vectorizing the matrix \mathbf{Z} finally yields the general model of the virtual MIMO array signal in a given delay-Doppler cell under test, denoted as

$$\begin{aligned} \mathbf{z} &= (\mathbf{R}_x \otimes \mathbf{I}_{M_R}) \sum_{k=1}^{K_0} \alpha_k \mathbf{a}_T(\theta_k) \otimes \mathbf{a}_R(\theta_k) \\ &\quad + (\mathbf{R}_x \otimes \mathbf{I}_{M_R}) \sum_{k=1}^{K_1} \beta_{k,1} \mathbf{a}_T(\vartheta_k) \otimes \mathbf{a}_R(\varphi_k) \\ &\quad + (\mathbf{R}_x \otimes \mathbf{I}_{M_R}) \sum_{k=1}^{K_1} \beta_{k,2} \mathbf{a}_T(\varphi_k) \otimes \mathbf{a}_R(\vartheta_k) \\ &\quad + \mathbf{r}, \end{aligned} \quad (6)$$

where $\mathbf{R}_x = \mathbf{X}^* \mathbf{X}^T$, $\mathbf{r} = ((\mathbf{X}^* \mathbf{P}(f_d)) \otimes \mathbf{I}_{M_R}) \tilde{\mathbf{w}}$, $\tilde{\mathbf{w}} = \text{vec}(\mathbf{W})$. Denoting $\Theta_0 = [\theta_1, \theta_2, \dots, \theta_{K_0}]^T \in \mathbb{R}^{K_0 \times 1}$ as the vector containing the angles of K_0 direct paths, the corresponding steering matrix is $\mathbf{A}(\Theta_0) = [\mathbf{a}(\theta_1), \mathbf{a}(\theta_2), \dots, \mathbf{a}(\theta_{K_0})] \in \mathbb{C}^{M_T M_R \times K_0}$ where $\mathbf{a}(\cdot) = \mathbf{a}_T(\cdot) \otimes \mathbf{a}_R(\cdot)$. In the absence of first-order paths ($K_1 = 0$), the signal model in (6) simplifies to

$$\mathbf{z} = (\mathbf{R}_x \otimes \mathbf{I}_{M_R}) \mathbf{A}(\Theta_0) \boldsymbol{\alpha} + \mathbf{r}, \quad (7)$$

where $\boldsymbol{\alpha} = [\alpha_1, \alpha_2, \dots, \alpha_{K_0}]^T \in \mathbb{C}^{K_0 \times 1}$ is the amplitude vector of direct paths.

In the presence of first-order paths ($K_1 \neq 0$), we define the DOD angle vector $\Theta_1 = [\vartheta_1, \vartheta_2, \dots, \vartheta_{K_1}]^T \in \mathbb{R}^{K_1 \times 1}$, the DOA angle vector $\Phi_1 = [\varphi_1, \varphi_2, \dots, \varphi_{K_1}]^T \in \mathbb{R}^{K_1 \times 1}$ and the amplitude vector $\beta_1 = [\beta_{1,1}, \beta_{2,1}, \dots, \beta_{K_1,1}, \beta_{1,2}, \beta_{2,2}, \dots, \beta_{K_1,2}]^T \in \mathbb{C}^{2K_1 \times 1}$ for the K_1 pair of first-order paths. Moreover, we define $\Theta = [\Theta_1^T, \Phi_1^T, \Theta_0^T]^T \in \mathbb{R}^{(2K_1 + K_0) \times 1}$, $\Phi = [\Phi_1^T, \Theta_1^T, \Theta_0^T]^T \in \mathbb{R}^{(2K_1 + K_0) \times 1}$. Denoting \mathbf{A}_T and \mathbf{A}_R as steering matrices of the radar TX and RX arrays, respectively, we have

$$\begin{aligned} \mathbf{A}_T(\Theta) &= [\mathbf{a}_T(\vartheta_1), \dots, \mathbf{a}_T(\vartheta_{K_1}), \mathbf{a}_T(\varphi_1), \dots, \mathbf{a}_T(\varphi_{K_1}), \\ &\quad \mathbf{a}_T(\theta_1), \dots, \mathbf{a}_T(\theta_{K_0})], \\ \mathbf{A}_R(\Phi) &= [\mathbf{a}_R(\varphi_1), \dots, \mathbf{a}_R(\varphi_{K_1}), \mathbf{a}_R(\vartheta_1), \dots, \mathbf{a}_R(\vartheta_{K_1}), \\ &\quad \mathbf{a}_R(\theta_1), \dots, \mathbf{a}_R(\theta_{K_0})], \end{aligned}$$

and the signal model (6) can be rewritten as

$$\mathbf{z} = (\mathbf{R}_x \otimes \mathbf{I}_{M_R}) \mathbf{A}(\Theta, \Phi) \boldsymbol{\beta} + \mathbf{r}, \quad (8)$$

In the previous equation $\mathbf{A}(\Theta, \Phi) = \mathbf{A}_T(\Theta) \circ \mathbf{A}_R(\Phi)$ denotes the response matrix, $\boldsymbol{\beta} = [\beta_1^T, \boldsymbol{\alpha}^T]^T \in \mathbb{C}^{(2K_1 + K_0) \times 1}$ is

the complex amplitude vector. Note that a pair of first-order paths share the same sparse pattern which is usually smaller than the number of array elements [23], resulting in a group-sparse structure that can be employed for multipath estimation purpose.

III. DETECTION OF MULTIPATH

In the general setup outlined in the previous section, ghost detection amounts to solving a coupled detection-estimation problem, wherein we have to discriminate between a composite hypothesis, \mathcal{H}_0 say, that the observations only contain a *unknown* number K_0 of direct paths coming from as many *unknown* different directions, against a *composite* alternative, \mathcal{H}_1 say, that the observations also contain a *unknown* number K_1 of first-order paths each characterized by an unknown pair of angles. In what follows, we (suboptimally) break up this problem into a two-step procedure: first, we introduce and discuss a GLRT assuming that the number of the direct and first-order paths, as well as the corresponding angular information - i.e., the matrices $\mathbf{A}(\Theta_0)$ of (7) and $\mathbf{A}(\Theta, \Phi)$ of (8) - are *known*. Subsequently, we illustrate a number of possible techniques to provide the detector with the required information (i.e., we make it *implementable*), by formulating the problem of preliminary estimating these matrices as a sparse recovery problem taking full advantage of the models introduced in the previous section.

A. GLRT Detector

Assume at first that the two matrices in (7) and (8) are known, whereby we have to solve the *composite* binary hypothesis test

$$\begin{cases} \mathcal{H}_0 : \mathbf{z} = (\mathbf{R}_x \otimes \mathbf{I}_{M_R}) \mathbf{A}(\Theta_0) \boldsymbol{\alpha} + \mathbf{r}, \\ \mathcal{H}_1 : \mathbf{z} = (\mathbf{R}_x \otimes \mathbf{I}_{M_R}) \mathbf{A}(\Theta, \Phi) \boldsymbol{\beta} + \mathbf{r}, \end{cases} \quad (9)$$

where $\boldsymbol{\alpha} \in \mathbb{C}^{K_0 \times 1}$ and $\boldsymbol{\beta} \in \mathbb{C}^{(K_0 + 2K_1) \times 1}$ are *unknown* parameters. Before proceeding, it is worth commenting on some constraints we want to force upon the solution of the above test, i.e.:

- 1) We want the test to be Constant False Alarm Rate (CFAR), i.e. its test statistic pdf under \mathcal{H}_0 and its detection threshold to be *functionally independent* of the noise floor and of the directions and intensities of the direct paths;
- 2) We want the resulting test to have some form of *optimality*, so as to use its performance as a yardstick to compare our implementable solutions to.

Since

$$\begin{aligned} \mathbb{E}(\mathbf{r}\mathbf{r}^H) &= \mathbb{E}((\mathbf{X}^* \otimes \mathbf{I}_{M_R}) \tilde{\mathbf{w}} \tilde{\mathbf{w}}^H (\mathbf{X}^* \otimes \mathbf{I}_{M_R})^H) \\ &= (\mathbf{X}^* \otimes \mathbf{I}_{M_R}) \sigma^2 \mathbf{I}_{M_R L} (\mathbf{X}^T \otimes \mathbf{I}_{M_R}) \\ &= \sigma^2 (\mathbf{X}^* \mathbf{X}^T) \otimes \mathbf{I}_{M_R} \\ &= \sigma^2 \mathbf{R}_x \otimes \mathbf{I}_{M_R}, \end{aligned} \quad (10)$$

we have $\mathbf{r} \sim \mathcal{CN}(\mathbf{0}, \sigma^2 \boldsymbol{\Sigma}_x)$ where $\boldsymbol{\Sigma}_x = \mathbf{R}_x \otimes \mathbf{I}_{M_R}$. From now on, we assume $\text{rank}(\mathbf{R}_x) = \text{rank}(\mathbf{X}) = M_T^1$, the correlation matrix $\boldsymbol{\Sigma}_x$ is also full-rank. Since $\boldsymbol{\Sigma}_x$ is known, a noise-whitening transformation converts the test (9) into

$$\begin{aligned} H_0 : \bar{\mathbf{z}} &\sim \mathcal{CN}(\boldsymbol{\Sigma}_x^{1/2} \mathbf{A}(\boldsymbol{\Theta}_0) \boldsymbol{\alpha}, \sigma^2 \mathbf{I}_{M_T M_R}), \\ H_1 : \bar{\mathbf{z}} &\sim \mathcal{CN}(\boldsymbol{\Sigma}_x^{1/2} \mathbf{A}(\boldsymbol{\Theta}, \boldsymbol{\Phi}) \boldsymbol{\beta}, \sigma^2 \mathbf{I}_{M_T M_R}), \end{aligned} \quad (11)$$

where $\bar{\mathbf{z}} = \boldsymbol{\Sigma}_x^{-1/2} \mathbf{z}$. Notice that, by construction, $\boldsymbol{\Sigma}_x^{1/2} \mathbf{A}(\boldsymbol{\Theta}, \boldsymbol{\Phi})$ is the matrix concatenation [41]

$$\boldsymbol{\Sigma}_x^{1/2} \mathbf{A}(\boldsymbol{\Theta}, \boldsymbol{\Phi}) = \boldsymbol{\Sigma}_x^{1/2} [\mathbf{E}, \mathbf{A}(\boldsymbol{\Theta}_0)], \quad (12)$$

where $\mathbf{E} = [\mathbf{A}(\boldsymbol{\Theta}_1, \boldsymbol{\Phi}_1), \mathbf{A}(\boldsymbol{\Phi}_1, \boldsymbol{\Theta}_1)] \in \mathbb{C}^{M_T M_R \times 2K_1}$ only depends on the DODs and the DOAs of the first-order paths. Under the CFAR constraint outlined above, we are thus in the situation of detecting a subspace signal in subspace interference and noise of unknown level [41, Section VIII], whereby the GLRT reads

$$\mathcal{T}_{GLRT} = \frac{\|\mathbf{P}(\boldsymbol{\Theta}_0) \bar{\mathbf{z}}\|^2}{\|\mathbf{P}(\boldsymbol{\Theta}, \boldsymbol{\Phi}) \bar{\mathbf{z}}\|^2} \underset{\mathcal{H}_0}{\overset{\mathcal{H}_1}{\geq}} \lambda_G, \quad (13)$$

where $\mathbf{P}(\boldsymbol{\Theta}_0) = \mathbf{I}_{M_T M_R} - \boldsymbol{\Sigma}_x^{1/2} \mathbf{A}(\boldsymbol{\Theta}_0) (\boldsymbol{\Sigma}_x^{1/2} \mathbf{A}(\boldsymbol{\Theta}_0))^\dagger = \mathbf{P}_0$ is the orthogonal projector onto the orthogonal complement of $\boldsymbol{\Sigma}_x^{1/2} \mathbf{A}(\boldsymbol{\Theta}_0)$ in $\mathbb{C}^{M_T M_R}$, and $\mathbf{P}(\boldsymbol{\Theta}, \boldsymbol{\Phi}) = \mathbf{P}_1$ has the same meaning with respect to $\boldsymbol{\Sigma}_x^{1/2} \mathbf{A}(\boldsymbol{\Theta}, \boldsymbol{\Phi})$, λ_G is the detection threshold.

The test (13), which we adopt outright, complies with the prior constraints 1) and 2). Concerning 1), indeed, the test is *invariant* to transformations that rotate the observations in the range span of $\mathbf{G} = \mathbf{P}_0 \boldsymbol{\Sigma}_x^{1/2} \mathbf{E}$ and positively *scale* $\bar{\mathbf{z}}$ [41]. As we'll be shortly verifying, this results in a detection threshold and a false alarm probability which are independent of both $\mathbf{A}(\boldsymbol{\Theta}_0)$ and the noise floor σ^2 . Concerning optimality, the test statistic in (13) turns out to be a *maximal invariant* statistic [42], whereby the test (13) is Uniformly Most Powerful (UMP) one under the said invariance constraints.

B. Performance Bounds and Waveform Optimization

In this section, we first specialize on the problem at hand the key results of [41, Section VIII] concerning the detection performance of the test family (13), and then we deal with the optimization of the transmit space-time code matrix. Since $\boldsymbol{\Sigma}_x^{1/2} \mathbf{A}(\boldsymbol{\Theta}, \boldsymbol{\Phi})$ is a concatenation of $\boldsymbol{\Sigma}_x^{1/2} \mathbf{A}(\boldsymbol{\Theta}_0)$ with some \mathbf{E} , we have that $\mathcal{R}(\boldsymbol{\Sigma}_x^{1/2} \mathbf{A}(\boldsymbol{\Theta}_0)) \subseteq \mathcal{R}(\boldsymbol{\Sigma}_x^{1/2} \mathbf{A}(\boldsymbol{\Theta}, \boldsymbol{\Phi}))$, whereby $\mathcal{R}(\mathbf{P}_1) \subseteq \mathcal{R}(\mathbf{P}_0)$, i.e. $\mathcal{R}(\mathbf{P}_0) = \mathcal{R}(\mathbf{P}_1) \oplus \mathcal{S}_\perp$, where \mathcal{S}_\perp denotes the orthogonal complement of $\mathcal{R}(\mathbf{P}_1)$ in $\mathcal{R}(\mathbf{P}_0)$. Denoting $\mathbf{P}^{\mathcal{S}_\perp}$ as the orthogonal projector onto \mathcal{S}_\perp , and assuming that the echo signals from different paths are incoherent, we have $\dim(\mathcal{R}(\mathbf{P}_1)) = M_T M_R - K_0 - 2K_1$, $\dim(\mathcal{R}(\mathbf{P}_0)) = M_T M_R - K_0$ and $\dim(\mathcal{R}(\mathbf{P}^{\mathcal{S}_\perp})) = 2K_1$, leading to [41, Section VIII]

$$\frac{\|\mathbf{P}_0 \bar{\mathbf{z}}\|^2}{\|\mathbf{P}_1 \bar{\mathbf{z}}\|^2} = 1 + \frac{\|\mathbf{P}^{\mathcal{S}_\perp} \bar{\mathbf{z}}\|^2}{\|\mathbf{P}_1 \bar{\mathbf{z}}\|^2} = 1 + X. \quad (14)$$

¹A justification of this assumption will be given infra.

Under \mathcal{H}_0 , X is the ratio of two independent central Chi-square random variables, with $4K_1$ and $2(M_T M_R - K_0 - 2K_1)$ degrees of freedom, respectively, and hence has a Fisher-Snedecor distribution with density

$$f_{X|\mathcal{H}_0}(x) = \frac{1}{B(2K_1; m)} x^{2K_1-1} (1+x)^{-(m+2K_1)}, \quad (15)$$

where $m = M_T M_R - K_0 - 2K_1$ and $B(a; b)$ denotes the beta function with parameters a and b .

In order to determine the density under \mathcal{H}_1 , a model for $\boldsymbol{\beta}$ is to be chosen. A customary assumption is that $\boldsymbol{\beta} \sim \mathcal{CN}(0, \mathbf{K}_\beta)$, namely that it is a proper complex Gaussian vector with covariance matrix \mathbf{K}_β , which implies that the test statistic has again a Fisher-Snedecor distribution [41, Section VIII]. Since

$$\begin{aligned} \mathbb{E} \left(\left\| \mathbf{P}^{\mathcal{S}_\perp} \bar{\mathbf{z}} \right\|^2 \middle| \mathcal{H}_1 \right) &= \mathbb{E} \left(\left\| \mathbf{P}^{\mathcal{S}_\perp} \boldsymbol{\Sigma}_x^{1/2} \mathbf{A}(\boldsymbol{\Theta}, \boldsymbol{\Phi}) \boldsymbol{\beta} + \mathbf{P}^{\mathcal{S}_\perp} \mathbf{r} \right\|^2 \right) \\ &= \text{Tr} \left(\mathbf{E}^H \boldsymbol{\Sigma}_x^{1/2} \mathbf{P}_0 \boldsymbol{\Sigma}_x^{1/2} \mathbf{E} \mathbf{K}_\beta \right) + \sigma^2 2K_1, \end{aligned} \quad (16)$$

we have

$$\begin{aligned} f_{X|\mathcal{H}_1}(x) &= \frac{1}{(1+\rho_1)B(2K_1; m)} \left(\frac{x}{1+\rho_1} \right)^{2K_1-1} \\ &\quad \times \left(1 + \frac{x}{1+\rho_1} \right)^{-(m+2K_1)}, \end{aligned} \quad (17)$$

where

$$\rho_1 = \frac{\text{Tr} \left(\mathbf{E}^H \boldsymbol{\Sigma}_x^{1/2} \mathbf{P}_0 \boldsymbol{\Sigma}_x^{1/2} \mathbf{E} \mathbf{K}_\beta \right)}{2K_1 \sigma^2}. \quad (18)$$

Elementary calculations allow thus to determine the performance of the test in the form:

$$P_{\text{fa}} = 1 - \frac{1}{B(2K_1; m)} \sum_{i=0}^{m-1} \frac{(-1)^i \binom{m-1}{i}}{2K_1 + i} \left(1 - \frac{1}{\lambda_G} \right)^{2K_1+i}, \quad (19)$$

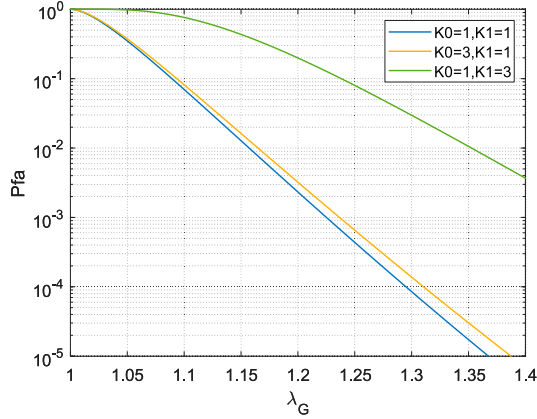
$$P_{\text{d}} = 1 - \frac{1}{B(2K_1; m)} \sum_{i=0}^{m-1} \frac{(-1)^i \binom{m-1}{i}}{2K_1 + i} \left(\frac{\lambda_G - 1}{\lambda_G + \rho_1} \right)^{2K_1+i}. \quad (20)$$

As far as the false alarm performance is concerned, we recall here that the test (13) achieves CFARness, whereby P_{fa} only depends on K_0 and K_1 : sample plots of the behavior of P_{fa} versus the threshold for some values of K_0 and K_1 are reported in Fig. 2.

Concerning the detection probability, we refer to the interesting special case that $\boldsymbol{\beta} \sim \mathcal{CN}(0, \sigma_\beta^2 \mathbf{I}_{2K_1})$, $\boldsymbol{\alpha} \sim \mathcal{CN}(0, \sigma_\alpha^2 \mathbf{I}_{K_0})$, which yields

$$\begin{aligned} \rho_1 &= \frac{\sigma_\beta^2}{2K_1 \sigma^2} \text{Tr} \left(\mathbf{E}^H \boldsymbol{\Sigma}_x^{1/2} \mathbf{P}_0 \boldsymbol{\Sigma}_x^{1/2} \mathbf{E} \right) = \frac{\sigma_\beta^2}{2K_1 \sigma^2} \\ &\quad \times \text{Tr} \left(\mathbf{E}^H \boldsymbol{\Sigma}_x \mathbf{E} - \mathbf{E}^H \boldsymbol{\Sigma}_x \mathbf{A}_0 (\mathbf{A}_0^H \boldsymbol{\Sigma}_x \mathbf{A}_0)^{-1} \mathbf{A}_0^H \boldsymbol{\Sigma}_x \mathbf{E} \right), \end{aligned} \quad (21)$$

where $\mathbf{A}_0 = \mathbf{A}(\boldsymbol{\Theta}_0)$. The quantity in (21) represents a suitable figure of merit to be maximized over the set of admissible code matrices under additional constraints, so as to endow the


 Fig. 2. P_{fa} versus λ_G with $M_T M_R = 48$.

resulting waveform with relevant features. The first constraint is obviously a power constraint, expressed as $\mathbf{x}_m^H \mathbf{x}_m = 1$, where \mathbf{x}_m represents the code sequence of the m -th transmitter for $m = 1, 2, \dots, M_T$. Notice also that, in the presence of some prior information on the surrounding environment, a reasonable constraint should be $\|\mathbf{R}_x - \mathbf{V}\|^2 \leq \epsilon$ where \mathbf{V} is a proper beamforming matrix that accounts for prior information on the angular location of real and virtual sources. If no such information is available, then we need to robustify the design, by avoiding the radar has blind angles, whereby we force the condition that \mathbf{R}_x should not be too far from the ‘‘orthogonal form’’ which ensures complete coverage of all the angles. As a consequence, the optimization problem to be solved reads

$$\begin{aligned} & \max_{\Sigma_x} \text{Tr} \left(\mathbf{E}^H \Sigma_x \mathbf{E} - \mathbf{E}^H \Sigma_x \mathbf{A}_0 (\mathbf{A}_0^H \Sigma_x \mathbf{A}_0)^{-1} \mathbf{A}_0^H \Sigma_x \mathbf{E} \right) \\ & \text{s.t. } [\mathbf{R}_x]_{m,m} = 1, m = 1, 2, \dots, M_T \\ & \quad \|\mathbf{R}_x - \mathbf{I}_{M_T}\|^2 \leq \mu \quad \Sigma_x \succeq \mathbf{0}, \end{aligned}$$

with $\Sigma_x = \mathbf{R}_x \otimes \mathbf{I}_{M_R}$. Notice that, since $\mathbf{\Pi} \succeq \mathbf{B}$ implies $\text{Tr}(\mathbf{\Pi}) \geq \text{Tr}(\mathbf{B})$, the problem

$$\max_{\mathbf{\Pi}} -\text{Tr}(\mathbf{\Pi}) \quad \text{s.t. } \mathbf{\Pi} \succeq \mathbf{B}$$

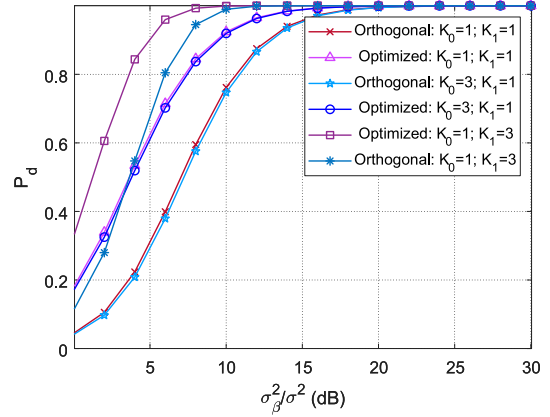
admits $\text{Tr}(\mathbf{\Pi}) = \text{Tr}(\mathbf{B})$ as unique solution. Thus maximizing the objective function in (21) boils down to solving the problem

$$\begin{aligned} & \max_{\Sigma_x, \mathbf{\Pi}} \left[\text{Tr} \left(\mathbf{E}^H \Sigma_x \mathbf{E} \right) - \text{Tr}(\mathbf{\Pi}) \right] \\ & \mathbf{\Pi} \succeq \mathbf{E}^H \Sigma_x \mathbf{A}_0 (\mathbf{A}_0^H \Sigma_x \mathbf{A}_0)^{-1} \mathbf{A}_0^H \Sigma_x \mathbf{E} \end{aligned}$$

The constraint is obviously satisfied since the Schur complement of the matrix

$$\Lambda = \begin{bmatrix} \mathbf{\Pi} & \mathbf{E}^H (\mathbf{R}_x \otimes \mathbf{I}_{M_R}) \mathbf{A}_0 \\ \mathbf{A}_0^H (\mathbf{R}_x \otimes \mathbf{I}_{M_R}) \mathbf{E} & (\mathbf{A}_0^H (\mathbf{R}_x \otimes \mathbf{I}_{M_R}) \mathbf{A}_0) \end{bmatrix}$$

with respect to the block $(\mathbf{A}_0^H (\mathbf{R}_x \otimes \mathbf{I}_{M_R}) \mathbf{A}_0)$ is semi-definite positive, and the matrix $\mathbf{\Pi}$ is necessarily also positive semi-definite. As a consequence, waveform optimization reduces to


 Fig. 3. P_d versus $\sigma_\beta^2 / \sigma^2$ with $M_T M_R = 48$.

solving the convex problem

$$\begin{aligned} & \arg \max_{\mathbf{R}_x, \mathbf{\Pi}} \text{Tr} \left(\mathbf{E}^H (\mathbf{R}_x \otimes \mathbf{I}_{M_R}) \mathbf{E} - \mathbf{\Pi} \right) \\ & \text{s.t. } [\mathbf{R}_x]_{m,m} = 1, m = 1, 2, \dots, M_T \\ & \quad \mathbf{\Lambda} \succeq \mathbf{0} \\ & \quad \|\mathbf{R}_x - \mathbf{I}_{M_T}\|^2 \leq \mu \\ & \quad \mathbf{R}_x \succeq \mathbf{0}. \end{aligned} \quad (22)$$

Since (22) is a Semi-Definite Programming (SDP) problem, it can be solved efficiently by the convex optimization approach. Fig. 3 highlights the detector behavior for different values of (K_0, K_1) and the impact of the number of system degrees of freedom $M_T M_R$. Not surprisingly, we observe that larger values of K_1 for fixed K_0 result in better detection performance. This is obviously because the two subspaces defined by the projection matrices \mathbf{P}_0 and \mathbf{P}_1 become more and more distinguishable as K_1 increases: the inevitable consequence is that the ‘‘worst case’’ is the situation where K_0 is large (in the plot, $K_0 = 3$) and K_1 small (in the plot, $K_1 = 1$). In this figure, two types of waveforms are compared including the orthogonal waveform with $\mathbf{R}_x = \mathbf{I}_{M_T}$, the optimized waveform with the perfect parameter information of direct and first-order paths. By optimizing the transmit waveform, a significant improvement in target detection performance can be achieved.

IV. ANGLE ESTIMATION FOR MULTIPATHS

As anticipated, the test (13) is not implementable, in that the two matrices $\mathbf{A}(\Theta_0)$ and $\mathbf{A}(\Theta, \Phi)$ are not known even in their order. In principle, such a prior uncertainty could be addressed within the GLRT framework. Noticing that directly solving the problems $\min_{K_0, \mathbf{A}(\Theta_0) \in \mathbb{C}^{M_T M_R \times K_0}} \|\mathbf{P}(\Theta_0) \bar{\mathbf{z}}\|^2$ and $\min_{K_0, K_1, \mathbf{A}(\Theta, \Phi) \in \mathbb{C}^{M_T M_R \times (K_0 + 2K_1)}} \|\mathbf{P}(\Theta, \Phi) \bar{\mathbf{z}}\|^2$ leads to an overestimation of the model order. To address this, we introduce the sparsity of the reflection paths for estimating $\mathbf{A}(\Theta_0)$ and $\mathbf{A}(\Theta, \Phi)$. This sparsity can be justified by the fact that automotive radar systems, typically equipped with an array configuration of at least 3 transmitters and 4 receivers (i.e. $M_T M_R > 12$), utilize mm-wave technology with a wide

bandwidth for high range resolution. As a result, only a limited number of targets, usually fewer than three, are present within the same delay-Doppler bin [6], meaning K_0 and K_1 are usually much smaller than $M_T M_R$ [43]. Specifically, we try to resolve the following problem assuming \mathcal{H}_0 hypothesis is true:

$$\begin{aligned} (\hat{K}_0, \hat{\Theta}_0, \hat{\alpha}) &= \arg \min_{\Theta_0 \in \mathbb{R}^{K_0 \times 1}, \alpha \in \mathbb{C}^{K_0 \times 1}, K_0} K_0 \\ \text{s.t. } & \|\bar{\mathbf{z}} - \bar{\mathbf{A}}(\Theta_0)\alpha\|_2^2 \leq \epsilon^2, \end{aligned} \quad (23)$$

where $\bar{\mathbf{A}}(\cdot) = \sum_x^{1/2} \mathbf{A}(\cdot)$, and obtain a suitable estimation of the direct paths $\hat{\Theta}_0$. It is worth noting that for any Θ_0 , α should be $\bar{\mathbf{A}}^\dagger(\Theta_0)\bar{\mathbf{z}}$ to minimize $\|\bar{\mathbf{z}} - \bar{\mathbf{A}}(\Theta_0)\alpha\|_2^2$, so the constraints degrades to $\|\mathbf{P}(\Theta_0)\bar{\mathbf{z}}\|_2^2 \leq \epsilon$.

Similarly, assuming \mathcal{H}_1 hypothesis is true, we resort to:

$$\begin{aligned} (\hat{K}_0, \hat{K}_1, \hat{\Theta}, \hat{\Phi}, \hat{\beta}) &= \arg \min_{\substack{K_0, K_1, \\ \Theta \in \mathbb{R}^{(K_0+2K_1) \times 1}, \\ \Phi \in \mathbb{R}^{(K_0+2K_1) \times 1}, \\ \beta \in \mathbb{C}^{(K_0+2K_1) \times 1}}} K_0 + \delta K_1 \\ \text{s.t. } & \|\bar{\mathbf{z}} - \bar{\mathbf{A}}(\Theta, \Phi)\beta\|_2^2 \leq \epsilon^2, \end{aligned} \quad (24)$$

where δ is the parameter characterizing the weights between K_0 and K_1 . The test family is then applied for the detection of \mathcal{H}_1 from \mathcal{H}_0

$$\frac{\|(\mathbf{I}_{M_T M_R} - \bar{\mathbf{A}}(\hat{\Theta}_0)\bar{\mathbf{A}}^\dagger(\hat{\Theta}_0))\bar{\mathbf{z}}\|_2^2}{\|(\mathbf{I}_{M_T M_R} - \bar{\mathbf{A}}(\hat{\Theta}, \hat{\Phi})\bar{\mathbf{A}}^\dagger(\hat{\Theta}, \hat{\Phi}))\bar{\mathbf{z}}\|_2^2} \stackrel{\mathcal{H}_1}{\geq} \lambda_G. \quad (25)$$

The next two subsections are thus devoted to illustrating how the needed estimators may be designed to solve (23) and (24) through bounded-complexity procedures.

A. Estimators for Θ_0 Under \mathcal{H}_0 Hypothesis

We propose here an iterative procedure to solve (23). We define $\mathbf{r}^{(t)}$ as the residual in the t -th iteration, obtained by subtracting the contribution from the estimated angles at that iteration. It is initialized as $\mathbf{r}^{(0)} = \bar{\mathbf{z}}$. As to the set of the angles of the direct paths, it is initialized as the empty set, i.e. $\hat{\Theta}_0^{(0)} = \emptyset$ and $\hat{K}_0^{(0)} = 0$. The algorithm thus entails an initial search over a uniform grid of size G , $\{\hat{\theta}_1, \hat{\theta}_2, \dots, \hat{\theta}_G\}$ say, and successive refinement of the estimate in a continuous domain.

In the t -th iteration, we insert a path into the set and $\hat{K}_0^{(t)}$ is updated as $\hat{K}_0^{(t)} = \hat{K}_0^{(t-1)} + 1$. The minimization of the ℓ_2 -norm of the residual entails evaluating

$$\hat{\theta}^{(t)} = \arg \max_{\theta^{(t)} \in \{\hat{\theta}_1, \hat{\theta}_2, \dots, \hat{\theta}_G\}} \left| \left(\mathbf{r}^{(t-1)} \right)^H \mathbf{a}(\theta^{(t)}) \right|, \quad (26)$$

and updating the angle matrix as $\hat{\Theta}_0^{(t,0)} = [(\hat{\Theta}_0^{(t-1)})^T, \hat{\theta}^{(t)}]^T$. The accuracy of this estimate is subsequently enhanced by using Gauss-Newton (GN) iterations adopting the results of the on-grid search, i.e. $\hat{\Theta}_0^{(t,0)}$, as the initial point. The GN method thus updates such an estimate through the inner iteration

$$\hat{\Theta}_0^{(t,i+1)} = \hat{\Theta}_0^{(t,i)} - (\mathbf{H}_0^{(t,i)})^{-1} \mathbf{g}_0^{(t,i)}, \quad (27)$$

where $\mathbf{g}_0^{(t,i)}$ and $\mathbf{H}_0^{(t,i)}$ denoting gradient and Hessian of the function $F(\Theta_0^{(t,i)}) = \|\bar{\mathbf{z}} - \bar{\mathbf{A}}(\Theta_0^{(t,i)})\bar{\mathbf{A}}^\dagger(\Theta_0^{(t,i)})\bar{\mathbf{z}}\|_2^2$, respectively. Define $\bar{\mathbf{A}}_0^{(t,i)} = \bar{\mathbf{A}}(\Theta_0^{(t,i)})$, $\mathbf{P}_0^{(t,i)} = \mathbf{P}(\Theta_0^{(t,i)})$. Following the derivations in Appendix A, the expressions of $\mathbf{H}_0^{(t,i)}$ and $\mathbf{g}_0^{(t,i)}$ are given by

$$\mathbf{g}_0^{(t,i)} = -2\text{Re} \left\{ \text{diag} \left\{ \left(\bar{\mathbf{A}}_0^{(t,i)} \right)^\dagger \bar{\mathbf{z}} \bar{\mathbf{z}}^H \mathbf{P}_0^{(t,i)} \mathbf{D}_0^{(t,i)} \right\} \right\}, \quad (28)$$

$$\begin{aligned} \mathbf{H}_0^{(t,i)} &= 2\text{Re} \left\{ \left(\mathbf{D}_0^{(t,i)} \right)^H \mathbf{P}_0^{(t,i)} \mathbf{D}_0^{(t,i)} \right. \\ &\quad \odot \left(\left(\mathbf{A}_0^{(t,i)} \right)^\dagger \bar{\mathbf{z}} \bar{\mathbf{z}}^H \left(\left(\mathbf{A}_0^{(t,i)} \right)^\dagger \right)^H \right)^T \left. \right\} \\ &\quad + 2\text{Re} \left\{ \left(\mathbf{D}_0^{(t,i)} \right)^H \mathbf{P}_0^{(t,i)} \bar{\mathbf{z}} \bar{\mathbf{z}}^H \mathbf{P}_0^{(t,i)} \left(\mathbf{D}_0^{(t,i)} \right)^T \right. \\ &\quad \left. \odot \left(\left(\bar{\mathbf{A}}_0^{(t,i)} \right)^\dagger \left(\left(\bar{\mathbf{A}}_0^{(t,i)} \right)^\dagger \right)^H \right) \right\}, \end{aligned} \quad (29)$$

where $\mathbf{D}_0^{(t,i)} = \left[\frac{\partial \bar{\mathbf{a}}(\hat{\theta}_1^{(i)})}{\partial \hat{\theta}_1^{(i)}}, \frac{\partial \bar{\mathbf{a}}(\hat{\theta}_2^{(i)})}{\partial \hat{\theta}_2^{(i)}}, \dots, \frac{\partial \bar{\mathbf{a}}(\hat{\theta}_t^{(i)})}{\partial \hat{\theta}_t^{(i)}} \right]^T$ with $\bar{\mathbf{a}}(\hat{\theta}_j^{(i)}) = \sum_x^{1/2} \mathbf{a}(\hat{\theta}_j^{(i)})$ for $j = 1, 2, \dots, t$.

The above computations are carried out iteratively until a maximum iteration number I is reached, whereby $\hat{\Theta}_0^{(t,I)}$ is adopted as the refined estimated angle $\hat{\Theta}_0^{(t)}$ in the t -th iteration. This allows updating the amplitude estimates and the residual as:

$$\hat{\alpha}^{(t)} = \bar{\mathbf{A}}^\dagger(\hat{\Theta}_0^{(t)})\bar{\mathbf{z}}, \quad (30)$$

$$\mathbf{r}^{(t)} = \bar{\mathbf{z}} - \bar{\mathbf{A}}(\hat{\Theta}_0^{(t)})\hat{\alpha}^{(t)}. \quad (31)$$

In principle, the iterative process stops when $\|\mathbf{r}^{(t)}\|_2 \leq \epsilon$ i.e. the condition of (23) is satisfied. Additionally, considering the potential issue of overestimating K_0 , we also set a maximum number of iterations T . The iterative process will be terminated if $t \geq T$ or $\|\mathbf{r}^{(t-1)}\|_2 - \|\mathbf{r}^{(t)}\|_2 \leq \epsilon_1$. The detailed procedure is given in Algorithm 1 and we name the proposed method as Compressed Sensing method in Continuous Domain under hypothesis \mathcal{H}_0 (CSCD-H0) algorithm.

It is worth noticing that, without the refinement step, the algorithm would reduce to an Orthogonal Matching Pursuit (OMP) algorithm [44], which is a classic method in CS. As OMP does not involve grid refinement in the continuous domain, a simplification may cause a remarkable performance impairment due to the well-known off-grid problem and would likely lead to overestimating the value of K_0 .

B. Estimators for (Θ, Φ) Under \mathcal{H}_1 Hypothesis

Under \mathcal{H}_1 , the algorithm we propose is an extension of the previous one, on the understanding that now the angles of both direct and first-order paths must be estimated. To reduce interference between direct and first-order paths, we implement the estimation procedures separately on direct and first-order paths

Algorithm 1: CSCD-H0 algorithm

Input: $\bar{\mathbf{z}}, \{\hat{\theta}_1, \hat{\theta}_2, \dots, \hat{\theta}_G\}$ and $T, I, \epsilon, \epsilon_1$;
Output: $\hat{K}_0, \hat{\alpha} \in \mathbb{C}^{\hat{K}_0 \times 1}, \hat{\Theta}_0 \in \mathbb{R}^{\hat{K}_0 \times 1}$;
1 Initialization: $\hat{\Theta}_0^{(0)} = \emptyset$ and $\hat{K}_0^{(0)} = 0, \mathbf{r}^{(0)} = \bar{\mathbf{z}}, t = 0$;
2 while $\|\mathbf{r}^{(t)}\|_2 > \epsilon$ **do**
3 $t \leftarrow t + 1$;
4 Obtain the inserted angle $\hat{\theta}^{(t)}$ via (26);
5 $\hat{\Theta}_0^{(t,0)} = [(\hat{\Theta}_0^{(t-1)})^T, \hat{\theta}^{(t)}]^T, \hat{K}_0^{(t)} = \hat{K}_0^{(t-1)} + 1$;
6 **for** $i = 0$ **to** I **do**
7 Calculate $\mathbf{g}_0^{(t,i)}$ and $\mathbf{H}_0^{(t,i)}$ according to (28)
 and (29), respectively;
8 Update $\hat{\Theta}_0^{(t,i+1)}$ by (27);
9 **end**
10 Update $\hat{\Theta}_0^{(t)} \leftarrow \hat{\Theta}_0^{(t,I)}$,
11 Update $\hat{\alpha}^{(t)}$ and residue $\mathbf{r}^{(t)}$ by (30) and (31),
 respectively;
12 **if** $t \geq T$ or $\|\mathbf{r}^{(t-1)}\|_2 - \|\mathbf{r}^{(t)}\|_2 \leq \epsilon_1$ **then**
13 | Break;
14 **end**
15 end
16 Return: $\hat{\Theta}_0 = \hat{\Theta}_0^{(t)}, \hat{\alpha} = \hat{\alpha}^{(t)}, \hat{K}_0 = \hat{K}_0^{(t)}$.

and subsequently decide the estimated paths that should be retained. The initial values of the relevant parameters are of course $\mathbf{r}^{(0)} = \mathbf{z}, \hat{\Theta}_1^{(0)} = \emptyset, \hat{\Phi}_1^{(0)} = \emptyset, \hat{\Theta}_0^{(0)} = \emptyset, \hat{K}_1^{(0)} = 0, \hat{K}_0^{(0)} = 0$.

Assume we want to estimate an additional direct path. Again, we first undertake a search on a G -dimensional grid of the common values of its DOA and DOD according to (26), thus obtaining a coarse estimate of the angle set $\bar{\Theta}^{(t,0)} = [\bar{\Theta}_1^{(t,0)}; \bar{\Phi}_1^{(t,0)}; \bar{\Theta}_0^{(t,0)}]$ with $\bar{\Theta}_1^{(t,0)} = \hat{\Theta}_1^{(t-1)}, \bar{\Phi}_1^{(t,0)} = \hat{\Phi}_1^{(t-1)}$ and $\bar{\Theta}_0^{(t,0)} = [(\hat{\Theta}_0^{(t-1)})^T, \hat{\theta}^{(t)}]^T$.

In order to search for an additional first-order path pair, coarse estimates of the angle pair $(\hat{\vartheta}^{(t)}, \hat{\varphi}^{(t)})$ are again obtained via search on two uniform G -dimensional grids $\Xi_t = \{\hat{\vartheta}_1, \hat{\vartheta}_2, \dots, \hat{\vartheta}_G\}$ and $\Xi_r = \{\hat{\varphi}_1, \hat{\varphi}_2, \dots, \hat{\varphi}_G\}$:

$$\begin{aligned}
 & (\hat{\vartheta}^{(t)}, \hat{\varphi}^{(t)}) \\
 & = \arg \max_{\substack{\vartheta^{(t)} \in \Xi_t \\ \varphi^{(t)} \in \Xi_r \\ \vartheta^{(t)} < \varphi^{(t)}}} \left(|(\mathbf{r}^{(t-1)})^H (\mathbf{a}_T(\vartheta^{(t)}) \circ \mathbf{a}_R(\varphi^{(t)}))| \right. \\
 & \quad \left. + |(\mathbf{r}^{(t-1)})^H (\mathbf{a}_T(\varphi^{(t)}) \circ \mathbf{a}_R(\vartheta^{(t)}))| \right). \quad (32)
 \end{aligned}$$

We thus have a coarse estimate of the angle set $\bar{\Theta}^{(t,0)} = [\bar{\Theta}_1^{(t,0)}; \bar{\Phi}_1^{(t,0)}; \bar{\Theta}_0^{(t,0)}]$ with $\bar{\Theta}_1^{(t,0)} = [(\hat{\Theta}_1^{(t-1)})^T, \hat{\vartheta}^{(t)}]^T, \bar{\Phi}_1^{(t,0)} = [(\hat{\Phi}_1^{(t-1)})^T, \hat{\varphi}^{(t)}]^T$ and $\bar{\Theta}_0^{(t,0)} = \hat{\Theta}_0^{(t-1)}$. The refinement steps of the two estimates above via search on a continuous domain have the same rationale as for the case illustrated in the previous subsection. Due to the mixture of direct and first-order paths under the \mathcal{H}_1 hypothesis, the GN method may lead to unstable estimation due to the

rank-deficiency in Hessian when the difference between DOD and DOA is not large². Therefore, we resort to the LM method [45] for updating angle estimates.

For brevity, here we outline the LM iteration for the search of an additional direct path since the search for an additional first-order path follows the same flow with $\bar{\Theta}^{(t,0)}$ replaced by $\bar{\Theta}^{(t,i)}$. The angle set is updated as $\bar{\Theta}^{(t,i+1)} = \bar{\Theta}^{(t,i)} + \mathbf{h}^{(t,i)}$, where

$$\mathbf{h}^{(t,i)} = - \left(\mathbf{H}^{(t,i)} + \mu^{(t,i)} \mathbf{I}_{\hat{K}^{(t,i)}} \right)^{-1} \mathbf{g}^{(t,i)}, \quad (33)$$

with $\mathbf{H}^{(t,i)}$ and $\mathbf{g}^{(t,i)}$ denoting the Hessian and gradient of $\bar{F}(\bar{\Theta}^{(t,i)}) = \|\bar{\mathbf{z}} - \mathbf{A}(\bar{\Theta}^{(t,i)}, \bar{\Phi}^{(t,i)}) \mathbf{A}^\dagger(\bar{\Theta}^{(t,i)}, \bar{\Phi}^{(t,i)}) \bar{\mathbf{z}}\|_2^2$, respectively. $\hat{K}^{(t)}$ denotes the size of $\bar{\Theta}^{(t,i)}$, $\mu^{(t,i)}$ is a damping parameter. We emphasize that the quantities $\mathbf{g}^{(t,i)}$ and $\mathbf{H}^{(t,i)}$ are different from those under \mathcal{H}_0 . In fact, $\mathbf{g}^{(t,i)}$ should now be partitioned as:

$$\mathbf{g}^{(t,i)} = \left[\mathbf{g}_T^{(t,i)}; \mathbf{g}_R^{(t,i)}; \mathbf{g}_0^{(t,i)} \right], \quad (34)$$

where $\mathbf{g}_T^{(t,i)}$ and $\mathbf{g}_R^{(t,i)}$ denote the gradients of \bar{F} with respect to DOD's and DOA's of first-order paths, respectively, while $\mathbf{g}_0^{(t,i)}$ denotes the gradient of \bar{F} with respect to the DOA's of direct paths: closed-form expressions of these quantities are given in (44)–(46) of Appendix B. Similarly, the matrix $\mathbf{H}^{(t,i)}$ is written as

$$\mathbf{H}^{(t,i)} = \begin{bmatrix} \mathbf{H}_{TT}^{(t,i)} & \mathbf{H}_{TR}^{(t,i)} & \mathbf{H}_{T0}^{(t,i)} \\ \mathbf{H}_{RT}^{(t,i)} & \mathbf{H}_{RR}^{(t,i)} & \mathbf{H}_{R0}^{(t,i)} \\ \mathbf{H}_{0T}^{(t,i)} & \mathbf{H}_{0R}^{(t,i)} & \mathbf{H}_{00}^{(t,i)} \end{bmatrix}, \quad (35)$$

and explicit forms for the different blocks are given in (50)–(58) of Appendix B.

We explicitly note here that paths with unequal DOD and DOA are added in pairs by (32), namely, first-order paths always appear in a paired, group-sparse manner. This group-sparse characteristic is rare in the interference from direct paths or grating lobes caused by sparse linear array (SLA). When calculating derivatives in $\mathbf{g}^{(t,i)}$ and $\mathbf{H}^{(t,i)}$, the pairwise constraint of the first-order paths must be considered. For instance, when calculating the derivative of \bar{F} with respect to $\hat{\vartheta}^{(t)}$, the derivative of both $\mathbf{a}_T(\hat{\vartheta}^{(t)}) \circ \mathbf{a}_R(\hat{\varphi}^{(t)})$ and $\mathbf{a}_T(\hat{\varphi}^{(t)}) \circ \mathbf{a}_R(\hat{\vartheta}^{(t)})$ should be calculated. This allows the algorithm to leverage the group-sparsity of the first-order paths to enhance the estimation accuracy.

The damping parameter $\mu^{(t,i)}$ in (33) is selected by a line search algorithm that is controlled by the gain ratio

$$\rho^{(t,i)} = \frac{\bar{F}(\bar{\Theta}^{(t,i)}) - \bar{F}(\bar{\Theta}^{(t,i)} + \mathbf{h}^{(t,i)})}{\frac{1}{2} (\mathbf{h}^{(t,i)})^H (\mu^{(t,i)} \mathbf{h}^{(t,i)} - \mathbf{g}^{(t,i)})}. \quad (36)$$

Steps 9-14 in Algorithm 2 describe how this parameter is obtained.

Once the refinement step is over, we obtain the angle set $\bar{\Theta}^{(t,T)} = [\bar{\Theta}_1^{(t,I)}; \bar{\Phi}_1^{(t,I)}; \bar{\Theta}_0^{(t,I)}]$ and the residual $\mathbf{r}_1^{(t)}$ for the estimate of an additional direct path, and $\bar{\Theta}^{(t,T)} =$

²An example will be given to illustrate this problem.

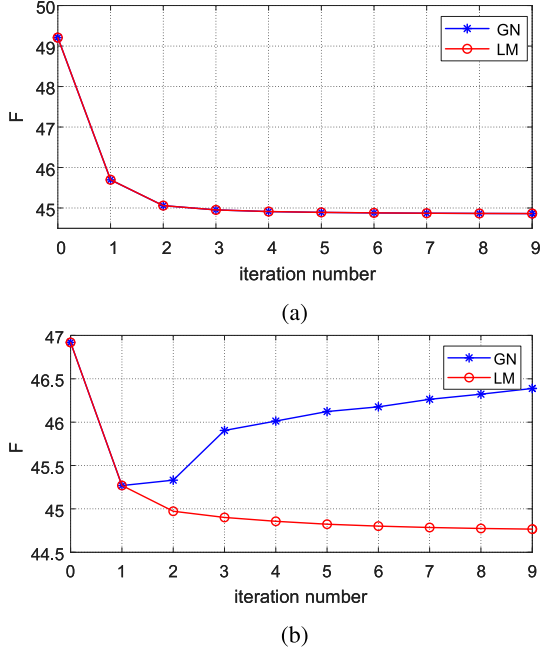


Fig. 4. Plots of cost function against the iteration number: (a) first-order path with $(-1.9^\circ, -13.2^\circ)$, (b) first-order path with $(-1.9^\circ, -3.2^\circ)$.

$[\bar{\Theta}_1^{(t,I)}; \bar{\Phi}_1^{(t,I)}; \bar{\Theta}_0^{(t,I)}]$ and $\mathbf{r}_2^{(t)}$ for the estimate of an additional pair of first-order paths. A decision on which model better fits the observation is thus made based on the quantity $r^{(t)} = \|\mathbf{r}_2^{(t)}\|_2 - \|\mathbf{r}_1^{(t)}\|_2$ through

$$(\hat{\Theta}_1^{(t)}, \hat{\Phi}_1^{(t)}, \hat{\Theta}_0^{(t)}) = \begin{cases} (\bar{\Theta}_1^{(t,I)}, \bar{\Phi}_1^{(t,I)}, \bar{\Theta}_0^{(t,I)}) & r^{(t)} > \delta_r \\ (\bar{\Theta}_1^{(t,I)}, \bar{\Phi}_1^{(t,I)}, \bar{\Theta}_0^{(t,I)}) & r^{(t)} < \delta_r \end{cases}$$

where δ_r is a suitably set threshold.

The proposed algorithm, named Compressed Sensing method in Continuous Domain under hypothesis \mathcal{H}_1 (CSCD-H1), is summarized in Algorithm 2 and, like CSCD-H0, reduces to a kind of Group OMP (GOMP) as the refinement phase is omitted.

We illustrate the convergence of the GN and LM methods implementation of the refined estimation through a simulation example. In Fig. 4, we compared the curves of the loss function F with the number of iterations during the optimization processes using both GN and LM methods. Specifically, Fig. 4(a) demonstrates similar convergence behavior for both methods in the scenarios with a large difference between DOD and DOA angles. However, when small differences between DOD and DOA angles are present, as shown in Fig. 4(b), the GN method faces challenges in achieving convergence. The instability of the GN method can be attributed to the rank-deficiency in the Hessian matrix. Conversely, the LM method incorporates a regularization term to address this problem and demonstrates more robustness in these scenarios.

Algorithm 2: CSCD-H1 algorithm

Input: $\bar{\mathbf{z}}, \bar{\Xi}_t, \bar{\Xi}_r$ and $T, I, J, \epsilon, \epsilon_2, \delta_r$;
Output: $\hat{K}_1, \hat{K}_0, \hat{\Theta}, \hat{\Phi}, \hat{\beta}$;

- 1 **Initialization:** $\hat{\Theta}_1^{(0)} = \emptyset, \hat{\Phi}_1^{(0)} = \emptyset, \hat{\Theta}_0^{(0)} = \emptyset,$
 $\mathbf{r}^{(0)} = \bar{\mathbf{z}}, t = 0;$
- 2 **while** $\|\mathbf{r}^{(t)}\|_2 > \epsilon$ **do**
- 3 $t \leftarrow t + 1;$
- 4 Obtain the angle of direct path $\hat{\theta}^{(t)}$ via (26);
- 5 Obtain $\bar{\Theta}^{(t,0)} = [\bar{\Theta}_1^{(t,0)}; \bar{\Phi}_1^{(t,0)}; \bar{\Theta}_0^{(t,0)}]$ where
 $\bar{\Theta}_1^{(t,0)} = \hat{\Theta}_1^{(t-1)}, \bar{\Phi}_1^{(t,0)} = \hat{\Phi}_1^{(t-1)}$ and
 $\bar{\Theta}_0^{(t,0)} = [(\hat{\Theta}_0^{(t-1)})^T, \hat{\theta}^{(t)}]^T;$
- 6 **for** $i = 0$ **to** I **do**
- 7 Calculate $\mathbf{g}^{(t,i)}$ and $\mathbf{H}^{(t,i)}$ using (34) and (35),
 respectively;
- 8 Calculate $\mathbf{h}^{(t,i)}$ and $\varrho^{(t,i)}$ by (33) and (36),
 respectively;
- 9 $j \leftarrow 0;$
- 10 **while** $\varrho^{(t,i)} \leq 0$ and $j < J$ **do**
- 11 Update $j \leftarrow j + 1, \mu^{(t,i)} \leftarrow 2^j \mu^{(t,i)};$
- 12 Calculate $\mathbf{h}^{(t,i)}$ and $\varrho^{(t,i)}$ by (33) and (36),
 respectively;
- 13 **end**
- 14 $\mu^{(t,i+1)} = \mu^{(t,i)} \max\{\frac{1}{3}, 1 - (2\varrho^{(t,i)} - 1)^3\};$
- 15 $\bar{\Theta}^{(t,i+1)} = \bar{\Theta}^{(t,i)} + \mathbf{h}^{(t,i)};$
- 16 **end**
- 17 $\mathbf{r}_1^{(t)} = \bar{\mathbf{z}} - \bar{\mathbf{A}}(\bar{\Theta}^{(t,I)}, \bar{\Phi}^{(t,I)})\bar{\mathbf{A}}^\dagger(\bar{\Theta}^{(t,I)}, \bar{\Phi}^{(t,I)})\bar{\mathbf{z}};$
- 18 Obtain the inserted angle pair $(\hat{\psi}^{(t)}, \hat{\varphi}^{(t)})$ via (32);
- 19 Obtain $\bar{\Theta}^{(t,0)} = [\bar{\Theta}_1^{(t,0)}; \bar{\Phi}_1^{(t,0)}; \bar{\Theta}_0^{(t,0)}]$ where
 $\bar{\Theta}_1^{(t,0)} = [(\hat{\Theta}_1^{(t-1)})^T, \hat{\psi}^{(t)}]^T, \bar{\Phi}_1^{(t,0)} =$
 $[(\hat{\Phi}_1^{(t-1)})^T, \hat{\varphi}^{(t)}]^T$ and $\bar{\Theta}_0^{(t,0)} = \hat{\Theta}_0^{(t-1)};$
- 20 Optimize the $\bar{\Theta}^{(t,0)}$ based on the LM method
 given by step 6 to step 16 with $\bar{\Theta}^{(t,0)}$ replaced
 by $\bar{\Theta}^{(t,0)};$
- 21 $\mathbf{r}_2^{(t)} = \bar{\mathbf{z}} - \bar{\mathbf{A}}(\bar{\Theta}^{(t,I)}, \bar{\Phi}^{(t,I)})\bar{\mathbf{A}}^\dagger(\bar{\Theta}^{(t,I)}, \bar{\Phi}^{(t,I)})\bar{\mathbf{z}};$
- 22 Calculate $r^{(t)} = \|\mathbf{r}_2^{(t)}\|_2 - \|\mathbf{r}_1^{(t)}\|_2;$
- 23 **if** $r^{(t)} < \delta_r$ **then**
- 24 $(\hat{\Theta}_1^{(t)}, \hat{\Phi}_1^{(t)}, \hat{\Theta}_0^{(t)}) = (\bar{\Theta}_1^{(t,I)}, \bar{\Phi}_1^{(t,I)}, \bar{\Theta}_0^{(t,I)});$
 $\mathbf{r}^{(t)} = \mathbf{r}_2^{(t)}.$
- 25 **else**
- 26 $(\hat{\Theta}_1^{(t)}, \hat{\Phi}_1^{(t)}, \hat{\Theta}_0^{(t)}) = (\bar{\Theta}_1^{(t,I)}, \bar{\Phi}_1^{(t,I)}, \bar{\Theta}_0^{(t,I)});$
 $\mathbf{r}^{(t)} = \mathbf{r}_1^{(t)}.$
- 27 **end**
- 28 **if** $t \geq T$ or $\|\mathbf{r}^{(t-1)}\|_2 - \|\mathbf{r}^{(t)}\|_2 \leq \epsilon_2$ **then**
- 29 Break;
- 30 **end**
- 31 **end**
- 32 **end**
- 33 **end**
- 34 **Return:** $\hat{\Theta} = [\hat{\Theta}_1^{(t)}, \hat{\Phi}_1^{(t)}, \hat{\Theta}_0^{(t)}], \hat{\Phi} = [\hat{\Phi}_1^{(t)}, \hat{\Theta}_1^{(t)}, \hat{\Theta}_0^{(t)}],$
 $\hat{\beta} = \bar{\mathbf{A}}^\dagger(\hat{\Theta}, \hat{\Phi})\bar{\mathbf{z}},$ length of $\hat{\Theta}_1^{(t)}$ as $\hat{K}_1,$ length of $\hat{\Theta}_0^{(t)}$
as \hat{K}_0

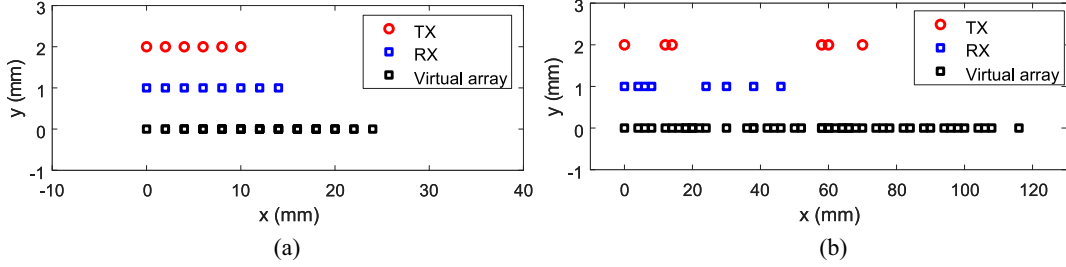


Fig. 5. Real and virtual layouts of the MIMO radar antennas, (a) ULA, (b) SLA.

V. SIMULATION AND EXPERIMENTAL RESULTS

A. Simulation Setup

In this section, numerical simulations are conducted to evaluate the performance of the proposed algorithm. For the proposed detection scheme, CSCD-H0 is adopted under \mathcal{H}_0 , and CSCD-H1 is adopted under \mathcal{H}_1 , so the detector is named GLRT-CSCD for simplicity. Likewise, we have GLRT-OMP algorithms for the detectors with OMP-based estimators. We include the IAA-based and the least absolute shrinkage and selection operator (LASSO)-based methods in the GLRT test, denoting them as GLRT-IAA and GLRT-LASSO, respectively.

Note that the angle estimation is crucial for the detection performance, we compare the accuracy of different methods. We conduct comparisons between the OMP, IAA [46], and LASSO [47] methods against our proposed CSCD-H0 algorithm in \mathcal{H}_0 scenario. Similarly, we evaluate the performance of the GOMP, multipath IAA (MPIAA) [28], and group LASSO (GLASSO) [48] methods against our proposed CSCD-H1 algorithm in \mathcal{H}_1 scenario. With the estimated angle, GLRT is applied to detect whether the first-order indirect path exists.

Other simulation parameters are set as follows:

- 1) The radar operates at 79 GHz with carrier wavelength $\lambda = 3.8$ mm. The number of transmitting elements $M_T = 6$ and receive element $M_R = 8$. We first conduct simulations with a uniform linear array (ULA) as illustrated in Fig. 5(a). Moreover, by maintaining constant values for M_T and M_R , we ensure a consistent upper bound in detection performance and subsequently verify the performance of an SLA as shown in Fig. 5(b).
- 2) The noise is randomly generated according to a Gaussian distribution with the variance $\sigma^2 = 1$. The path amplitudes are generated according to $\beta \sim \mathcal{CN}(0, \sigma_\beta^2 \mathbf{I}_{2K_1})$, $\alpha \sim \mathcal{CN}(0, \sigma_\alpha^2 \mathbf{I}_{K_0})$. The signal-to-noise-ratio (SNR) of direct paths and first-order paths are defined as σ_α^2/σ^2 and σ_β^2/σ^2 , respectively.
- 3) The grids are obtained by discretizing angle space $[-90^\circ, 90^\circ]$ with a step of 2° . The max iteration of the OMP, GOMP, CSCD-H0 and CSCD-H1 estimator are set to $T = 10$. The stop criterion parameters are set as $I = 10$, $\epsilon = \sqrt{\sigma^2 M_T M_R}$, $\epsilon_1 = 0.4$ and $\epsilon_2 = 0$. For CSCD-H1, we set parameters $\delta_r = \sigma$ and $J = 3$. The iteration number of IAA in \mathcal{H}_0 and \mathcal{H}_1 hypothesis are both set to 5, the regularization parameter of LASSO estimators

are set as $2\sigma\sqrt{2\log G}$ in \mathcal{H}_0 and $2\sigma\sqrt{2\log(G^2)}$ in \mathcal{H}_1 , respectively.

- 4) We evaluate the root-mean-squared-error (RMSE) of the angle estimation for the proposed algorithms. Notice that the algorithms return a bunch of estimations, corresponding to either true paths or erroneous ones, and the paths cannot be detected if there is no estimation close to its direction. We thus refer to the RMSEs conditioned on the correct path estimation. In undertaking simulations, a path is declared to be correctly estimated if its estimation error is smaller than the array beamwidth. Specifically, the RMSEs of the first-order path and direct path are calculated by

$$\text{RMSE}_1 = \sqrt{\frac{\frac{1}{\text{MC}} \sum_{m=1}^{\text{MC}} \frac{1}{2|\Omega_1^m|} \left(\sum_{j \in \Omega_1^m} \left((\vartheta_j^{(m)} - \hat{\vartheta}_j^{(m)})^2 + (\varphi_j^{(m)} - \hat{\varphi}_j^{(m)})^2 \right) \right)}{}} \quad (37)$$

$$\text{RMSE}_0 = \sqrt{\frac{1}{\text{MC}} \sum_{m=1}^{\text{MC}} \frac{1}{|\Omega_0^m|} \sum_{j \in \Omega_0^m} (\theta_j^{(m)} - \hat{\theta}_j^{(m)})^2} \quad (38)$$

respectively, where MC is the number of runs, Ω_1^m and Ω_0^m are the index set of the identified first-order paths and direct path in the m -th simulation respectively; $|\cdot|$ denotes the cardinality of the input set; $\vartheta_j^{(m)}$, $\varphi_j^{(m)}$ are the DOD and DOA the j -th first-order path in the m -th run and $\theta_j^{(m)}$ is the DOA of j -th direct path, while $\hat{\vartheta}_j^{(m)}$, $\hat{\varphi}_j^{(m)}$ and $\hat{\theta}_j^{(m)}$ are the estimates, respectively.

- 5) The detection performance of the proposed GLRT detector is compared with the performance bound derived in Sec. III-B. Specifically, the upper bound of P_d is calculated by (20) under perfect angle estimation.
- 6) Unless specifically stated, the probability of false alarm is set to be 10^{-3} , and the numbers of independent trials used for simulating the probabilities of false alarm and detection are $100/P_{fa}$ and 10^4 , respectively.

B. Complexity Analysis

To evaluate the complexity of the proposed CSCD-based estimator, we consider the aforementioned grid-based

TABLE I
COMPLEXITY ANALYSIS

Scenario	Method	Computational Complexity
\mathcal{H}_0	CSCD-H0	$\mathcal{O}(GM_T M_R K_0 + K_0^2 (M_T M_R)^2 I)$
	OMP	$\mathcal{O}(GM_T M_R K_0)$
	IAA	$\mathcal{O}((G^2 M_T M_R + M_T M_R^3)J)$
	LASSO	$\mathcal{O}(G^2 M_T M_R + G^3)$
\mathcal{H}_1	CSCD-H1	$\mathcal{O}(G^2 M_T M_R U + U^2 (M_T M_R)^2 I)$
	GOMP	$\mathcal{O}(G^2 M_T M_R U)$
	MPIAA	$\mathcal{O}((G^4 M_T M_R + M_T M_R^3)J)$
	GLASSO	$\mathcal{O}(G^4 M_T M_R + G^6)$

methods comparison, i.e., the OMP-based, LASSO-based, and IAA-based estimators. In these comparisons, the continuous spatial space is discretized into G grid points in \mathcal{H}_0 scenario and G^2 grid points in \mathcal{H}_1 scenario. The overall computational complexity of the algorithms depends on the number of iterations and the computational complexity per iteration. For the CSCD-H0, the computational complexity of the coarse and the refined estimation are $\mathcal{O}(GM_T M_R)$ and $\mathcal{O}(K_0(M_T M_R)^2 I)$, respectively. The number of iterations is proportional to the number of direct paths K_0 . Therefore, the overall computational complexity is $\mathcal{O}(GM_T M_R K_0 + K_0^2 (M_T M_R)^2 I)$. For the CSCD-H1, the number of iterations is proportional to $U = K_1 + K_0$, the overall computational complexity is $\mathcal{O}(G^2 M_T M_R U + U^2 (M_T M_R)^2 I)$. The OMP-based estimators are simplified versions of CSCD without fine estimation. Therefore, the computational complexity is $\mathcal{O}(GM_T M_R K_0)$ under \mathcal{H}_0 and $\mathcal{O}(G^2 M_T M_R U)$ under \mathcal{H}_1 , respectively. For the IAA-based estimator, the overall computational complexity is $\mathcal{O}((G^2 M_T M_R + M_T M_R^3)J)$ under \mathcal{H}_0 and $\mathcal{O}((G^4 M_T M_R + M_T M_R^3)J)$ under \mathcal{H}_1 , where J denotes the number of iterations. For the LASSO-based estimator, the complexity is $\mathcal{O}(G^2 M_T M_R + G^3)$ under \mathcal{H}_0 and $\mathcal{O}(G^4 M_T M_R + G^6)$ under \mathcal{H}_1 . We summarize the computational complexity of these methods in Table I. It can be seen that the proposed method, due to the addition of refined angle estimation, has a slightly higher computational complexity than the OMP-based estimator, but it is significantly lower than that of the IAA-based and LASSO-based estimators. Moreover, we note that the computational complexity of the refined estimation in our proposed method is independent of grid density. We can achieve accurate estimation in the continuous domain with a coarser grid and a lower computational load through refined estimation.

C. Estimation Performance

In this subsection, we verify the estimation performance of the proposed CSCD-H0 and CSCD-H1 algorithms. In the ULA array, we check the accuracy of direct path estimation in \mathcal{H}_0 scenario and first-order path estimation in \mathcal{H}_1 scenario in Fig. 6(a) and Fig. 6(c). As expected, the RMSE of all estimators decreases as SNR grows, indicating that larger SNR leads to better accuracy in estimation. LASSO-based, IAA-based and

OMP-based estimators suffer from off-grid issues, so their accuracy is consistently worse than that of the proposed algorithm. We notice that when the sparsity decreases (K_0 of Fig. 6(a), or K_1 of Fig. 6(c) from 1 to 3), a decline in the accuracy could be observed. This phenomenon can be explained by many existing works in CS [43]: the CS-based estimators take advantage of the sparsity inside signal for estimation and the performance is getting worse as the sparsity decreases.

In the SLA array, we continue to observe that the proposed CSCD-based method exhibits improved angle estimation performance as the SNR increases. However, the RMSE of the OMP-based, IAA-based, and LASSO-based estimators remains largely unchanged in both \mathcal{H}_0 and \mathcal{H}_1 scenarios. This phenomenon can be attributed, in part, to our method of calculating RMSE. We assess accuracy based on (37) and (38), considering only paths that have been correctly identified, with estimation errors smaller than the array beamwidth. The on-grid methods experience a decrease in the rate of correctly identified paths compared to the ULA array, and they are constrained by grid resolution, which makes it challenging for RMSE to improve with increasing SNR.

However, unlike the ULA with half-lambda separation, the basis of the SLA array could have a large correlation. In Fig. 7(a), given a direct path $\theta = 10^\circ$, we computed its correlation $\langle \mathbf{a}(\theta), \mathbf{a}(\psi) \rangle$ with the basis $\psi \in [-90^\circ, 90^\circ]$ and observe that SLA has a narrower beamwidth but higher sidelobes. Given a first-order path $(\vartheta, \varphi) = (10^\circ, -10^\circ)$, the correlation $\langle \mathbf{a}_T(\vartheta) \circ \mathbf{a}_R(\varphi), \mathbf{a}(\psi) \rangle$ are plotted in Fig. 7(b), where a distinct peak can be observed in SLA even if the signals are not matched. It indicates that, in SLA, the algorithm could make a mistake when doing basis selection and the performance of GLRT could be affected as well.

D. Detection Performance

In order to assess the detection performance of the proposed system, we need first to determine a method to set the detection threshold. In fact, unlike the ideal GLRT in (13), the GLRT-CSCD detector using CSCD-H0 and GCSH1 for estimation purposes no longer exhibits CFAR behavior, due to the inevitable errors occurring in the estimation procedures outlined in the previous section. It is thus necessary at first to undertake a sensitivity analysis, in order to assess if outright adoption of the detection threshold of the ideal GLRT, as defined in (19), yields a false alarm probability which at least preserves the order of magnitude of the designed value. To this end, we set a nominal value $P_{fa} = 10^{-3}$, select the corresponding detection threshold through inversion of (19), and then evaluate the false alarm probability achieved by the GLRT-LASSO, GLRT-IAA, GLRT-OMP and proposed GLRT-CSCD. The results are reported in Table II. Even though our analysis is far from being exhaustive, the results clearly show that the actual false alarm probability of GLRT-CSCD stays below the nominal level for a ULA configuration under all the inspected values of σ_α^2/σ^2 . The SLA configuration appears a little less favorable, especially as K_0 increases. This is due to the higher sidelobes that such an array configuration generates, with a consequent ‘‘spillover’’ of the

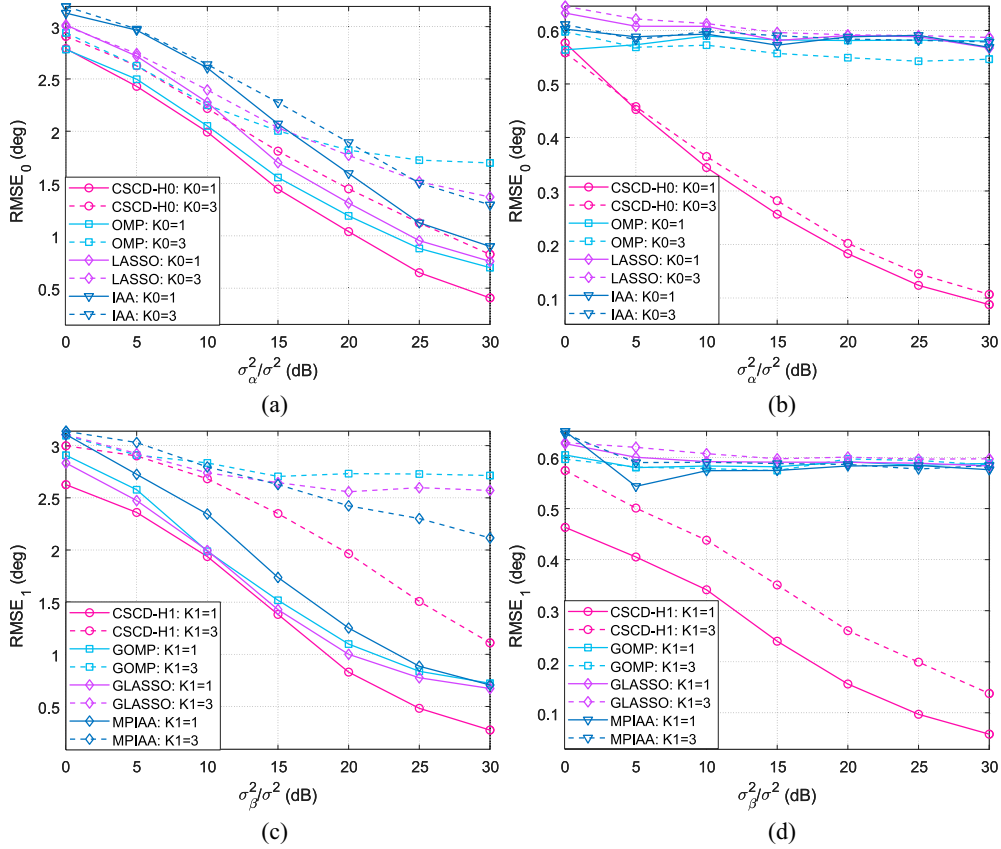
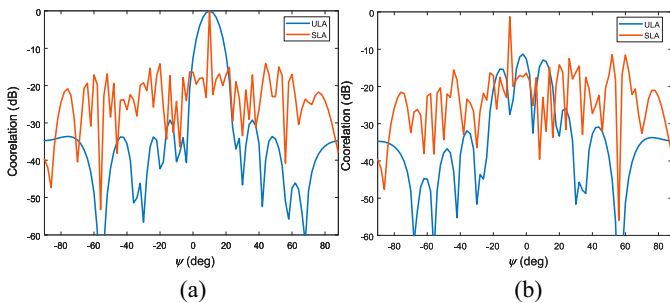

 Fig. 6. Plots of RMSE: (a) RMSE₀ in ULA, (b) RMSE₀ in SLA, (c) RMSE₁ in ULA, (d) RMSE₁ in SLA.

 TABLE II
 SIMULATION OF P_{fa} WITH $M_T M_R = 48$

Array	K_0	GLRT-CSCD		GLRT-OMP		GLRT-LASSO		GLRT-IAA	
		$\frac{\sigma_\alpha^2}{\sigma^2} = 0$ dB	$\frac{\sigma_\alpha^2}{\sigma^2} = 20$ dB	$\frac{\sigma_\alpha^2}{\sigma^2} = 0$ dB	$\frac{\sigma_\alpha^2}{\sigma^2} = 20$ dB	$\frac{\sigma_\alpha^2}{\sigma^2} = 0$ dB	$\frac{\sigma_\alpha^2}{\sigma^2} = 20$ dB	$\frac{\sigma_\alpha^2}{\sigma^2} = 0$ dB	$\frac{\sigma_\alpha^2}{\sigma^2} = 20$ dB
ULA	1	1.74×10^{-4}	3.00×10^{-5}	9.80×10^{-3}	2.30×10^{-3}	2.10×10^{-3}	5.40×10^{-3}	1.36×10^{-2}	2.64×10^{-3}
	3	3.00×10^{-4}	1.00×10^{-5}	5.80×10^{-3}	7.00×10^{-4}	1.12×10^{-3}	3.90×10^{-3}	1.44×10^{-2}	3.94×10^{-3}
SLA	1	4.50×10^{-4}	1.50×10^{-4}	2.12×10^{-2}	2.02×10^{-2}	1.05×10^{-3}	2.18×10^{-1}	1.08×10^{-2}	2.39×10^{-1}
	3	8.50×10^{-4}	5.30×10^{-4}	1.68×10^{-2}	5.70×10^{-3}	4.00×10^{-4}	1.64×10^{-1}	1.00×10^{-2}	2.41×10^{-1}


 Fig. 7. Comparison of (a) $\langle \mathbf{a}(\theta), \mathbf{a}(\psi) \rangle$ in \mathcal{H}_0 scenario, and (b) $\langle \mathbf{a}_T(\vartheta) \circ \mathbf{a}_R(\varphi), \mathbf{a}(\psi) \rangle$ in \mathcal{H}_1 scenario.

direct paths into the first-order path subspace, but the order of magnitude of the actual P_{fa} is again preserved. For the GLRT-OMP and GLRT-LASSO algorithms, the false alarm probability for both ULA and SLA is higher. And in the SLA, the order of magnitude of the actual P_{fa} can no longer be preserved. Also, we have observed a significant increase in the case of GLRT-IAA method in SLA scenarios. The worst P_{fa} is found in GLRT-IAA, at which point neither ULA nor SLA retains the magnitude of P_{fa} .

In Fig. 8, the P_d of GLRT-LASSO, GLRT-IAA, GLRT-OMP, and GLRT-CSCD are compared with the upper bound. For the ULA results given by Fig. 8(a), the detection performance of GLRT-CSCD with $K_1 = 1$ is close to the upper bound. As

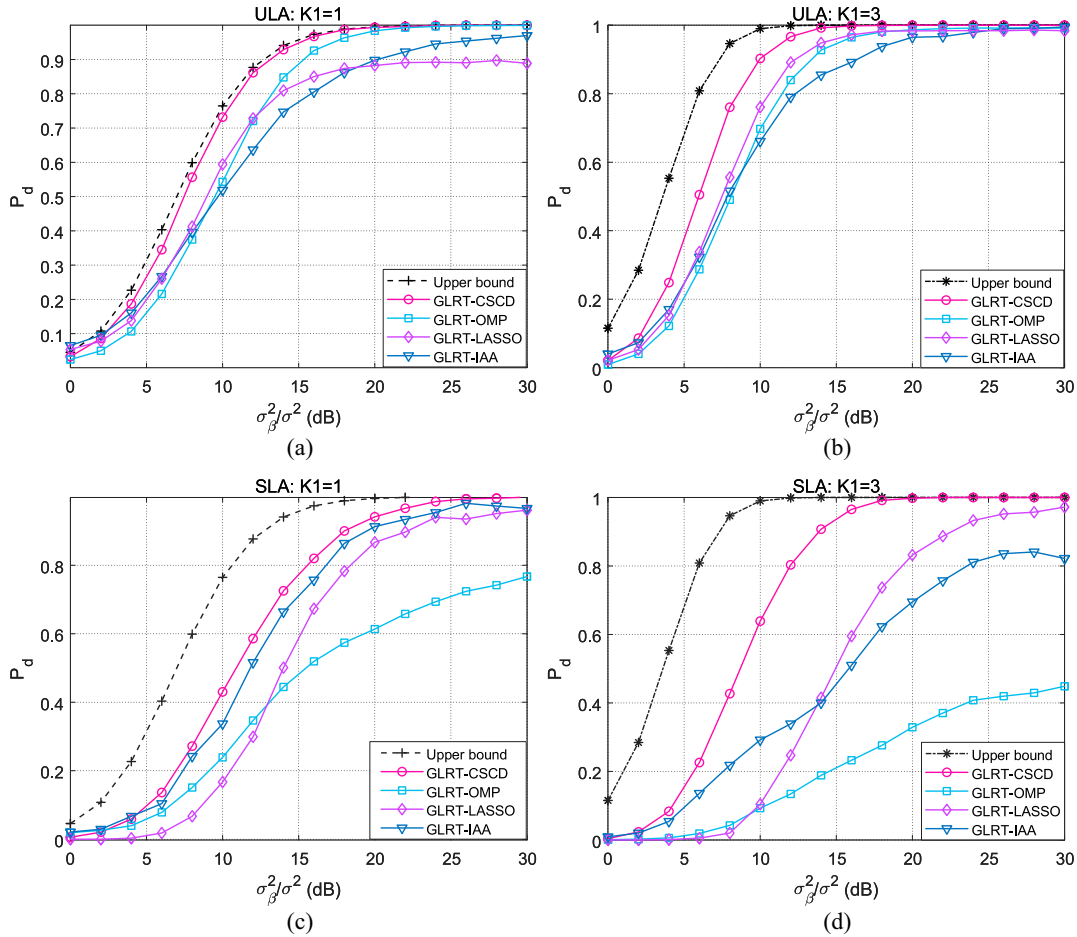


Fig. 8. P_d versus σ_β^2/σ^2 for ULA with (a) $K_1 = 1$ and (b) $K_1 = 3$, SLA with (c) $K_1 = 1$ and (d) $K_1 = 3$.

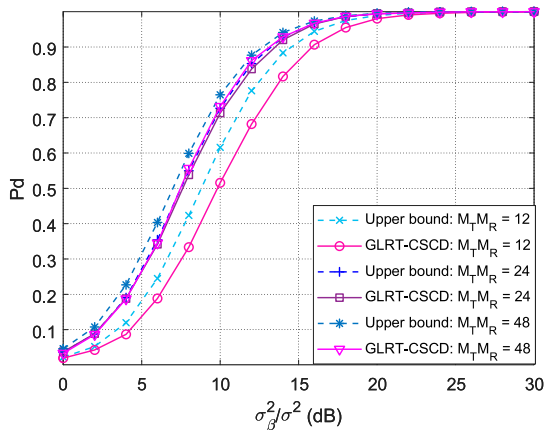


Fig. 9. P_d versus σ_β^2/σ^2 for different $M_T M_R$.

$K_1 = 3$ in Fig. 8(b), the performance gap between the proposed detectors and the upper bound becomes larger due to the degradation in estimation performance. This is also validated by our RMSE simulation given by Fig. 6(c). In the SLA, we can see from Fig. 8(b), that the discrepancy between the proposed detectors and the upper bound is larger than that of

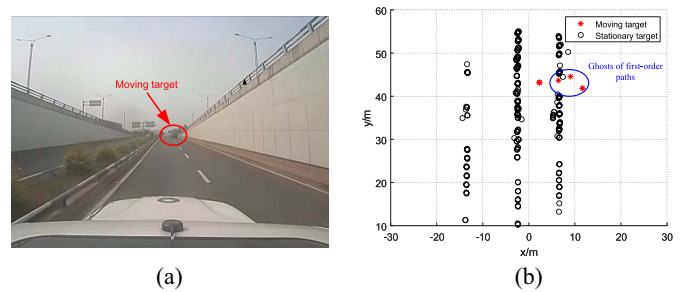


Fig. 10. Experimental scenario, (a) photograph of the experimental scenario, (b) points clouds with blue ellipse indicating ghosts induced by first-order paths.

ULA. The proposed GLRT-CSCD still benefits from a larger K_1 to achieve better detection performance. However, the angle estimation performance of the LASSO, IAA and OMP are much worse than that of the proposed algorithm, so its detection performance is considerably below the upper bound.

To compare detection performance across different array sizes, we set up simulations with $M_T = 3, M_R = 4$ ($M_T M_R = 12$), $M_T = 4, M_R = 6$ ($M_T M_R = 24$) and $M_T = 6, M_R = 8$

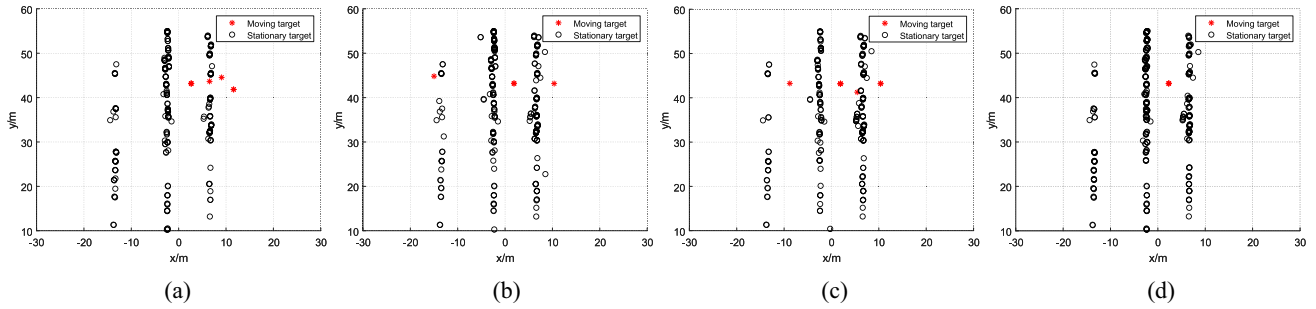


Fig. 11. Detection and elimination of ghost targets using (a) GLRT-OMP, (b) GLRT-LASSO, (c) GLRT-IAA and (d) GLRT-CSCD.

($M_T M_R = 48$). For simplicity, we adopt ULAs with half-wavelength element spacing and the detection performances are evaluated when $K_0 = 1$ and $K_1 = 1$. As reported in Fig. 9, the simulated performance is close to the upper bound given by the theoretical analysis. Detection performance improves with more degrees of freedom, even though the gain rapidly decreases once $M_T M_R$ is made sufficiently large as compared to the values of K_0 and K_1 .

E. Experimental Results

Next, we evaluate the target detection performance of the proposed detector by using the experimental data. The data are obtained by a millimeter-wave $f_0 = 77$ GHz MIMO radar where $M_T = 8$ transmitting antenna and $M_R = 16$ receiving antenna, all evenly spaced. The spacing at the transmitter side is 4.5λ , and the spacing at the receiver side is 4λ . Fig. 10(a) displays a typical automotive radar driving environment, where the road is flanked by concrete walls. The target is situated between these reflective surfaces, leading to multipath propagation of its echoes. Considering that the vehicle is in motion and all targets have a non-zero Doppler shift, to distinguish between stationary and moving targets in the scene, automotive radar can utilize the vehicle's speed by an Inertial Measurement Unit (IMU). The IMU calculates the vehicle's velocity by measuring linear acceleration and angular velocity. Then, based on the estimated angle of the detection point, its relative radial velocity is projected along the direction of the vehicle's velocity. If the projected velocity matches the vehicle's own speed, the detection point is identified as a stationary target; otherwise, it is from a moving target. However, as illustrated in Fig. 10(b), ghosts caused by multipath lead to mismatches, resulting in the appearance of moving ghost targets, significantly impacting the vehicle's perception and decision-making process.

In Fig. 11, we employ the aforementioned GLRT-OMP, GLRT-LASSO, GLRT-IAA, and the proposed GLRT-CSCD to detect and eliminate ghost targets. It can be observed that the GLRT-OMP, GLRT-LASSO, and GLRT-IAA methods fail to successfully remove all ghost targets in the scene, they inadvertently remove some direct paths from stationary targets. In contrast, the proposed GLRT-CSCD method effectively eliminates all ghost targets while preserving the direct paths of stationary targets.

VI. CONCLUSION

In this paper, we investigate the detection of ghost targets for automotive radar in the presence of multipaths. The existence of indirect paths is modeled as a binary composite hypothesis test and a GLRT detector is proposed to determine whether indirect paths exist in a delay-Doppler cell. If a cell contains indirect paths, the ghost targets could be removed and the desired direct paths can be preserved. Based on the theoretical analysis of the detection performance of GLRT under perfect angle estimation, we have derived a convex waveform optimization approach that can enhance detection performance. Considering practical scenarios with unknown angles of both direct and indirect paths, we propose a sparsity-enforced CS approach to estimate the angular parameters in the continuous domain. Simulation results indicate that the proposed algorithm outperforms on-grid estimators, thereby leading to better detection performance. The false alarm rate of the proposed detector could be controlled and the detection performance is close to the theoretical bound in the ULA case. Finally, the experimental results demonstrate the effectiveness of the proposed method.

APPENDIX

A. Derivation of \mathbf{g}_0 in (28) and \mathbf{H}_0 in (29)

For clarity, we drop the superscript (t, i) and input variable of the functions in some of the following derivation, i.e. $F = F(\hat{\Theta}_0^{(t,i)})$ and $\bar{\mathbf{A}}_0 = \bar{\mathbf{A}}(\hat{\Theta}_0^{(t,i)})$.

Denote $F = \mathbf{f}^H \mathbf{f}$ with $\mathbf{f} = \bar{\mathbf{z}} - \bar{\mathbf{A}} \bar{\mathbf{A}}^\dagger \bar{\mathbf{z}}$, the gradient of F with respect to $\Theta_0 \in \mathbb{R}^{K_0 \times 1}$ can be calculated by

$$\mathbf{g}_0 = \left[\frac{\partial F}{\partial \theta_1}, \frac{\partial F}{\partial \theta_2}, \dots, \frac{\partial F}{\partial \theta_{K_0}} \right]^T, \quad (39)$$

where the q -th element $[\mathbf{g}_0]_q$ given as $\frac{\partial F}{\partial \theta_q} = 2\text{Re}((\frac{\partial \mathbf{f}}{\partial \theta_q})^H \mathbf{f})$. Following the derivation in [49], we obtain

$$[\mathbf{g}_0]_q = -2\text{Re} \left\{ \text{Tr} \left\{ \bar{\mathbf{A}}_0^\dagger \bar{\mathbf{z}} \bar{\mathbf{z}}^H \mathbf{P}_0 \bar{\mathbf{A}}_q \right\} \right\}, \quad (40)$$

where $\bar{\mathbf{A}}_q = \frac{\partial \bar{\mathbf{A}}_0}{\partial \theta_q} = [\mathbf{0}, \mathbf{0}, \dots, \frac{\partial \bar{\mathbf{a}}}{\partial \theta_q}, \dots, \mathbf{0}]$ with $\frac{\partial \bar{\mathbf{a}}}{\partial \theta_q} = \frac{\partial \bar{\mathbf{a}}(\theta_q)}{\partial \theta_q}$.

The Hessian \mathbf{H}_0 denotes approximate second order partial derivative of F with respect to Θ_0 . In this matrix, the (q, p) -th element is denoted as $[\mathbf{H}_0]_{q,p} = 2\text{Re} \left\{ \left(\frac{\partial \mathbf{f}}{\partial \theta_q} \right)^H \frac{\partial \mathbf{f}}{\partial \theta_p} \right\}$ and can

be calculated as follows

$$\begin{aligned} [\mathbf{H}_0]_{q,p} &= 2\text{Re} \left\{ \text{Tr} \left\{ \bar{\mathbf{A}}_p \bar{\mathbf{A}}_0^\dagger \bar{\mathbf{z}} \bar{\mathbf{z}}^H (\bar{\mathbf{A}}_0^\dagger)^H \bar{\mathbf{A}}_q^H \mathbf{P}_0 \right\} \right. \\ &\quad \left. + 2\text{Re} \left\{ \text{Tr} \left\{ \bar{\mathbf{A}}_p^H \mathbf{P}_0 \bar{\mathbf{z}} \bar{\mathbf{z}}^H \mathbf{P}_0 \bar{\mathbf{A}}_q \bar{\mathbf{A}}_0^\dagger (\bar{\mathbf{A}}_0^\dagger)^H \right\} \right\}. \end{aligned} \quad (41)$$

Defining a partial matrix $\mathbf{D}_0 = \left[\frac{\partial \bar{\mathbf{a}}}{\partial \theta_1}, \frac{\partial \bar{\mathbf{a}}}{\partial \theta_2}, \dots, \frac{\partial \bar{\mathbf{a}}}{\partial \theta_{K_0}} \right]$, then the matrix form of \mathbf{g} and \mathbf{H}_0 can be given by (28) and (29), respectively.

B. Derivation of \mathbf{g} 's in (34) and \mathbf{H} 's in (35)

For clarity, we drop the superscript and input variable of the functions in some of the following derivations, i.e. $\bar{F} = \bar{F}(\bar{\Theta}^{(t,i)})$ and $\bar{\mathbf{A}} = \bar{\mathbf{A}}(\bar{\Theta}^{(t,i)}, \bar{\Phi}^{(t,i)})$. In the following, we derive the matrix expression of \mathbf{g}_T and \mathbf{H}_{TT} , the derivation for \mathbf{g}_R , \mathbf{g}'_0 , \mathbf{H}_{TR} , \mathbf{H}_{RR} , \mathbf{H}_{RT} , \mathbf{H}_{0T} , \mathbf{H}_{T0} , \mathbf{H}_{R0} , \mathbf{H}_{0R} , \mathbf{H}_{00} follow similar arguments and are omitted for brevity.

Similar with (40), we know the q -th element of \mathbf{g}_T can be given as

$$\begin{aligned} [\mathbf{g}_T]_q &= -2\text{Re} \left\{ \text{Tr} \left\{ \bar{\mathbf{A}}^\dagger \bar{\mathbf{z}} \bar{\mathbf{z}}^H \mathbf{P}_1 \bar{\mathbf{A}}'_q \right\} \right\}, \\ &= -2\text{Re} \left\{ \text{Tr} \left\{ \Gamma \bar{\mathbf{A}}'_q \right\} \right\}, \end{aligned} \quad (42)$$

where $\Gamma = \bar{\mathbf{A}}^\dagger \bar{\mathbf{z}} \bar{\mathbf{z}}^H \mathbf{P}_1 \in \mathbb{C}^{(2K_1+K_0) \times M_T M_R}$, $\bar{\mathbf{A}}'_q = \frac{\partial \bar{\mathbf{A}}}{\partial \vartheta_q} = [\mathbf{0}, \mathbf{0}, \dots, \frac{\partial \mathbf{a}_1}{\partial \vartheta_q}, \dots, \mathbf{0}, \dots, \frac{\partial \mathbf{a}_2}{\partial \vartheta_q}, \dots, \mathbf{0}]$ with $\frac{\partial \mathbf{a}_1}{\partial \vartheta_q} = \sum_x \frac{1}{2} \frac{\partial \mathbf{a}_T(\vartheta_q) \otimes \mathbf{a}_R(\vartheta_q)}{\partial \vartheta_q}$ and $\frac{\partial \mathbf{a}_2}{\partial \vartheta_q} = \sum_x \frac{1}{2} \frac{\partial \mathbf{a}_T(\vartheta_q) \otimes \mathbf{a}_R(\vartheta_q)}{\partial \vartheta_q}$. We divide the matrix Γ into three submatrices, denoted as $\Gamma = [\Gamma_1, \Gamma_2, \Gamma_0]$, where $\Gamma_1, \Gamma_2 \in \mathbb{C}^{K_1 \times M_T M_R}$, $\Gamma_0 \in \mathbb{C}^{K_0 \times M_T M_R}$. Then (42) can be rewritten as

$$[\mathbf{g}_T]_q = -2\text{Re} \left\{ \Gamma_1^T(q) \left(\frac{\partial \mathbf{a}_1}{\partial \vartheta_q} \right)^T + \Gamma_2^T(q) \left(\frac{\partial \mathbf{a}_2}{\partial \vartheta_q} \right)^T \right\}, \quad (43)$$

where $\Gamma_1^T(q)$ and $\Gamma_2^T(q)$ denote the q row of Γ_1 and Γ_2 , respectively. Define two partial matrices: $\mathbf{D}_{T1} = \left[\frac{\partial \mathbf{a}_1}{\partial \vartheta_1}, \frac{\partial \mathbf{a}_1}{\partial \vartheta_2}, \dots, \frac{\partial \mathbf{a}_1}{\partial \vartheta_{K_1}} \right]$, $\mathbf{D}_{T2} = \left[\frac{\partial \mathbf{a}_2}{\partial \vartheta_2}, \frac{\partial \mathbf{a}_2}{\partial \vartheta_3}, \dots, \frac{\partial \mathbf{a}_2}{\partial \vartheta_{K_1}} \right]$. We can then obtain the matrix form of \mathbf{g}_T given by

$$\mathbf{g}_T = -2\text{Re} \{ \text{diag} \{ \Gamma_1 \mathbf{D}_{T1} + \Gamma_2 \mathbf{D}_{T2} \} \}. \quad (44)$$

Similarly, we define $\mathbf{D}_{R1} = \left[\frac{\partial \mathbf{a}_1}{\partial \varphi_1}, \frac{\partial \mathbf{a}_1}{\partial \varphi_2}, \dots, \frac{\partial \mathbf{a}_1}{\partial \varphi_{K_1}} \right]$, $\mathbf{D}_{R2} = \left[\frac{\partial \mathbf{a}_2}{\partial \varphi_2}, \frac{\partial \mathbf{a}_2}{\partial \varphi_3}, \dots, \frac{\partial \mathbf{a}_2}{\partial \varphi_{K_1}} \right]$ and $\mathbf{D}_0 = \left[\frac{\partial \bar{\mathbf{a}}}{\partial \theta_1}, \frac{\partial \bar{\mathbf{a}}}{\partial \theta_2}, \dots, \frac{\partial \bar{\mathbf{a}}}{\partial \theta_{K_0}} \right]$, and obtain

$$\mathbf{g}_R = -2\text{Re} \{ \text{diag} \{ \Gamma_1 \mathbf{D}_{R1} + \Gamma_2 \mathbf{D}_{R2} \} \}, \quad (45)$$

$$\mathbf{g}'_0 = -2\text{Re} \{ \text{diag} \{ \Gamma_0 \mathbf{D}_0 \} \}. \quad (46)$$

The Hessian \mathbf{H}_{TT} denotes second order partial derivative with respect to Θ_1 , in which the (q, p) -th element is

$$\begin{aligned} [\mathbf{H}_{TT}]_{q,p} &= 2\text{Re} \left\{ \text{Tr} \left\{ \bar{\mathbf{A}}'_p \bar{\mathbf{A}}^\dagger \bar{\mathbf{z}} \bar{\mathbf{z}}^H (\bar{\mathbf{A}}^\dagger)^H (\bar{\mathbf{A}}'_q)^H \mathbf{P}_1 \right\} \right. \\ &\quad \left. + 2\text{Re} \left\{ \text{Tr} \left\{ (\bar{\mathbf{A}}'_p)^H \mathbf{P}_1 \bar{\mathbf{z}} \bar{\mathbf{z}}^H \mathbf{P}_1 \bar{\mathbf{A}}'_q \bar{\mathbf{A}}^\dagger (\bar{\mathbf{A}}^\dagger)^H \right\} \right\}, \end{aligned} \quad (47)$$

where the first item

$$\begin{aligned} &\text{Tr} \left\{ \bar{\mathbf{A}}'_p \bar{\mathbf{A}}^\dagger \bar{\mathbf{z}} \bar{\mathbf{z}}^H (\bar{\mathbf{A}}^\dagger)^H (\bar{\mathbf{A}}'_q)^H \mathbf{P}_1 \right\} \\ &= \mathbf{S}_{p,q} \left(\frac{\partial \mathbf{a}_1}{\partial \vartheta_q} \right)^H \mathbf{P}_1 \frac{\partial \mathbf{a}_1}{\partial \vartheta_p} + [\mathbf{S}]_{p,q+K_1} \left(\frac{\partial \mathbf{a}_2}{\partial \vartheta_q} \right)^H \mathbf{P}_1 \frac{\partial \mathbf{a}_1}{\partial \vartheta_p} \\ &\quad + [\mathbf{S}]_{p+K_1,q} \left(\frac{\partial \mathbf{a}_1}{\partial \vartheta_q} \right)^H \mathbf{P}_1 \frac{\partial \mathbf{a}_2}{\partial \vartheta_p} \\ &\quad + [\mathbf{S}]_{p+K_1,q+K_1} \left(\frac{\partial \mathbf{a}_2}{\partial \vartheta_q} \right)^H \mathbf{P}_1 \frac{\partial \mathbf{a}_2}{\partial \vartheta_p} \end{aligned}$$

with $\mathbf{S} = \bar{\mathbf{A}}^\dagger \bar{\mathbf{z}} \bar{\mathbf{z}}^H (\bar{\mathbf{A}}^\dagger)^H$, and the second item can be rewritten as

$$\begin{aligned} &\text{Tr} \left\{ (\bar{\mathbf{A}}'_p)^H \mathbf{P}_1 \bar{\mathbf{z}} \bar{\mathbf{z}}^H \mathbf{P}_1 \bar{\mathbf{A}}'_q \bar{\mathbf{A}}^\dagger (\bar{\mathbf{A}}^\dagger)^H \right\} \\ &= [\mathbf{C}]_{q,p} \left(\frac{\partial \mathbf{a}_1}{\partial \vartheta_p} \right)^H \mathbf{X} \frac{\partial \mathbf{a}_1}{\partial \vartheta_q} + [\mathbf{C}]_{q+K_1,p} \left(\frac{\partial \mathbf{a}_1}{\partial \vartheta_p} \right)^H \mathbf{X} \frac{\partial \mathbf{a}_2}{\partial \vartheta_q} \\ &\quad + [\mathbf{C}]_{q,p+K_1} \left(\frac{\partial \mathbf{a}_2}{\partial \vartheta_p} \right)^H \mathbf{X} \frac{\partial \mathbf{a}_1}{\partial \vartheta_q} \\ &\quad + [\mathbf{C}]_{q+K_1,p+K_1} \left(\frac{\partial \mathbf{a}_2}{\partial \vartheta_p} \right)^H \mathbf{X} \frac{\partial \mathbf{a}_2}{\partial \vartheta_q} \end{aligned}$$

with $\mathbf{X} = \mathbf{P}_1 \bar{\mathbf{z}} \bar{\mathbf{z}}^H \mathbf{P}_1$ and $\mathbf{C} = \bar{\mathbf{A}}^\dagger (\bar{\mathbf{A}}^\dagger)^H$. To represent \mathbf{H}_{TT} in matrix form, we divide matrices \mathbf{S} and \mathbf{C} into

$$\mathbf{S} = \begin{bmatrix} \mathbf{S}_1 & \mathbf{S}_{10} \\ \mathbf{S}_{01} & \mathbf{S}_0 \end{bmatrix}, \quad (48)$$

$$\mathbf{C} = \begin{bmatrix} \mathbf{C}_1 & \mathbf{C}_{10} \\ \mathbf{C}_{01} & \mathbf{C}_0 \end{bmatrix}, \quad (49)$$

where $\mathbf{S}_1, \mathbf{C}_1 \in \mathbb{C}^{2K_1 \times 2K_1}$, $\mathbf{S}_{10}, \mathbf{C}_{10} \in \mathbb{C}^{2K_1 \times K_0}$, $\mathbf{S}_{01}, \mathbf{C}_{01} \in \mathbb{C}^{K_0 \times 2K_1}$ and $\mathbf{S}_0, \mathbf{C}_0 \in \mathbb{C}^{K_0 \times K_0}$. Then, we obtain

$$\begin{aligned} \mathbf{H}_{TT} &= 2\text{Re} \left\{ \mathbf{E}_h(\mathbf{D}_T)^H \mathbf{P}_1 \mathbf{D}_T \odot \mathbf{S}_1^T \mathbf{E}_h^T \right\} \\ &\quad + 2\text{Re} \left\{ \mathbf{E}_h((\mathbf{D}_T)^H \mathbf{X} \mathbf{D}_T)^T \odot \mathbf{C}_1 \mathbf{E}_h^T \right\}, \end{aligned} \quad (50)$$

where $\mathbf{E}_h = [\mathbf{I}_{K_1}, \mathbf{I}_{K_1}] \in \mathbb{R}^{K_1 \times 2K_1}$, $\mathbf{D}_T = [\mathbf{D}_{T1}, \mathbf{D}_{T2}]$. Similarly, we define $\mathbf{D}_R = [\mathbf{D}_{R1}, \mathbf{D}_{R2}]$ and obtain

$$\begin{aligned} \mathbf{H}_{TR} &= 2\text{Re} \left\{ \mathbf{E}_h(\mathbf{D}_T)^H \mathbf{P}_1 \mathbf{D}_R \odot \mathbf{S}^T \mathbf{E}_h^T \right\} \\ &\quad + 2\text{Re} \left\{ \mathbf{E}_h((\mathbf{D}_R)^H \mathbf{X} \mathbf{D}_T)^T \odot \mathbf{C} \mathbf{E}_h^T \right\}, \end{aligned} \quad (51)$$

$$\begin{aligned} \mathbf{H}_{RT} &= 2\text{Re} \left\{ \mathbf{E}_h(\mathbf{D}_R)^H \mathbf{P}_1 \mathbf{D}_T \odot \mathbf{S}_1^T \mathbf{E}_h^T \right\} \\ &\quad + 2\text{Re} \left\{ \mathbf{E}_h((\mathbf{D}_T)^H \mathbf{X} \mathbf{D}_R)^T \odot \mathbf{C}_1 \mathbf{E}_h^T \right\}, \end{aligned} \quad (52)$$

$$\begin{aligned} \mathbf{H}_{RR} &= 2\text{Re} \left\{ \mathbf{E}_h(\mathbf{D}_R)^H \mathbf{P}_1 \mathbf{D}_R \odot \mathbf{S}_1^T \mathbf{E}_h^T \right\} \\ &\quad + 2\text{Re} \left\{ \mathbf{E}_h((\mathbf{D}_R)^H \mathbf{X} \mathbf{D}_R)^T \odot \mathbf{C}_1 \mathbf{E}_h^T \right\}, \end{aligned} \quad (53)$$

$$\begin{aligned} \mathbf{H}_{T0} &= 2\text{Re} \left\{ \mathbf{E}_h((\mathbf{D}_T)^H \mathbf{P}_1 \mathbf{D}_0 \odot \mathbf{S}_{01}^T) \right\} \\ &\quad + 2\text{Re} \left\{ \mathbf{E}_h(((\mathbf{D}_0)^H \mathbf{X} \mathbf{D}_T)^T \odot \mathbf{C}_{10}) \right\}, \end{aligned} \quad (54)$$

$$\begin{aligned} \mathbf{H}_{R0} &= 2\text{Re} \left\{ \mathbf{E}_h((\mathbf{D}_R)^H \mathbf{P}_1 \mathbf{D}_0 \odot \mathbf{S}_{01}^T) \right\} \\ &\quad + 2\text{Re} \left\{ \mathbf{E}_h(((\mathbf{D}_0)^H \mathbf{X} \mathbf{D}_R)^T \odot \mathbf{C}_{10}) \right\}, \end{aligned} \quad (55)$$

$$\begin{aligned} \mathbf{H}_{0T} &= 2\text{Re} \left\{ ((\mathbf{D}_0)^H \mathbf{P}_1 \mathbf{D}_T \odot \mathbf{S}_{10}^T) \mathbf{E}_h^T \right\} \\ &\quad + 2\text{Re} \left\{ (((\mathbf{D}_T)^H \mathbf{X} \mathbf{D}_0)^T \odot \mathbf{C}_{01}) \mathbf{E}_h^T \right\}, \end{aligned} \quad (56)$$

$$\begin{aligned} \mathbf{H}_{0R} &= 2\text{Re} \left\{ ((\mathbf{D}_0)^H \mathbf{P}_1 \mathbf{D}_R \odot \mathbf{S}_{10}^T) \mathbf{E}_h^T \right\} \\ &\quad + 2\text{Re} \left\{ (((\mathbf{D}_R)^H \mathbf{X} \mathbf{D}_0)^T \odot \mathbf{C}_{01}) \mathbf{E}_h^T \right\}, \end{aligned} \quad (57)$$

$$\begin{aligned} \mathbf{H}_{00} &= 2\text{Re} \left\{ \mathbf{D}_0^H \mathbf{P}_1 \mathbf{D}_0 \odot \mathbf{S}_0^T \right\} \\ &\quad + 2\text{Re} \left\{ (\mathbf{D}_0^H \mathbf{X} \mathbf{D}_0)^T \odot \mathbf{C}_0 \right\}. \end{aligned} \quad (58)$$

REFERENCES

- [1] S. M. Patole, M. Torlak, D. Wang, and M. Ali, "Automotive radars: A review of signal processing techniques," *IEEE Signal Process. Mag.*, vol. 34, no. 2, pp. 22–35, 2017.
- [2] F. Engels, P. Heidenreich, A. M. Zoubir, F. K. Jondral, and M. Wintermantel, "Advances in automotive radar: A framework on computationally efficient high-resolution frequency estimation," *IEEE Signal Process. Mag.*, vol. 34, no. 2, pp. 36–46, Mar. 2017.
- [3] F. Roos, J. Bechter, C. Knill, B. Schweizer, and C. Waldschmidt, "Radar sensors for autonomous driving: Modulation schemes and interference mitigation," *IEEE Microw. Mag.*, vol. 20, no. 9, pp. 58–72, Sep. 2019.
- [4] C. Waldschmidt, J. Hasch, and W. Menzel, "Automotive radar—From first efforts to future systems," *IEEE J. Microw.*, vol. 1, no. 1, pp. 135–148, Jan. 2021.
- [5] J. Li and P. Stoica, "MIMO radar with colocated antennas," *IEEE Signal Process. Mag.*, vol. 24, no. 5, pp. 106–114, Sep. 2007.
- [6] S. Sun, A. P. Petropulu, and H. V. Poor, "MIMO radar for advanced driver-assistance systems and autonomous driving: Advantages and challenges," *IEEE Signal Process. Mag.*, vol. 37, no. 4, pp. 98–117, Jul. 2020.
- [7] X. Hu, Y. Li, M. Lu, Y. Wang, and X. Yang, "A multi-carrier-frequency random-transmission chirp sequence for TDM MIMO automotive radar," *IEEE Trans. Veh. Technol.*, vol. 68, no. 4, pp. 3672–3685, Apr. 2019.
- [8] A. Kamann, P. Held, F. Perras, P. Zaumseil, T. Brandmeier, and U. T. Schwarz, "Automotive radar multipath propagation in uncertain environments," in *Proc. 21st Int. Conf. Intell. Transp. Syst. (ITSC)*, 2018, pp. 859–864.
- [9] T. Visentin, J. Hasch, and T. Zwick, "Analysis of multipath and DOA detection using a fully polarimetric automotive radar," in *Proc. Eur. Radar Conf. (EURAD)*, 2017, pp. 45–48.
- [10] K. Sabet, A. Sabet, J. Kral, and C. Woischwill, "Hybrid computer simulation of automotive radar systems in high multipath environments," in *Proc. IEEE Int. Symp. Antennas Propag. North Amer. Radio Sci. Meeting*, Montreal, QC, Canada, Piscataway, NJ, USA: IEEE Press, Jul. 2020, pp. 1561–1562.
- [11] O. Longman, S. Villeval, and I. Bilik, "Multipath ghost targets mitigation in automotive environments," in *Proc. IEEE Radar Conf. (Radar-Conf21)*, Atlanta, GA, USA, Piscataway, NJ, USA: IEEE Press, May 2021, pp. 1–5.
- [12] M. Levy-Israel, I. Bilik, and J. Tabrikian, "MCRB on DOA estimation for automotive MIMO radar in the presence of multipath," *IEEE Trans. Aerosp. Electron. Syst.*, vol. 59, no. 5, pp. 4831–4843, Oct. 2023.
- [13] R. Feng, E. D. Greef, M. Rykunov, H. Sahli, S. Pollin, and A. Bourdoux, "Multipath ghost recognition for indoor MIMO radar," *IEEE Trans. Geosci. Remote Sens.*, vol. 60, pp. 1–10, 2022.
- [14] F. Roos, M. Sadeghi, J. Bechter, N. Appenrodt, J. Dickmann, and C. Waldschmidt, "Ghost target identification by analysis of the Doppler distribution in automotive scenarios," in *Proc. 18th Int. Radar Symp. (IRS)*, 2017, pp. 1–9.
- [15] X. Qiu, X. Zhang, K. Huo, and W. Jiang, "Quartic Riemannian adaptive regularization with cubics for radar waveform design," *IEEE Trans. Aerosp. Electron. Syst.*, vol. 59, no. 6, pp. 7514–7528, Dec. 2023.
- [16] W. Li, Q. Wan, Y. Zhi, H. Peng, and J. Mao, "A Fans-shaped beam antenna design for overcoming multipath effects for 77GHz FMCW-MIMO radar," in *Proc. IEEE MTT-S Int. Wireless Symp. (IWS)*, Nanjing, China, Piscataway, NJ, USA: IEEE Press, May 2021, pp. 1–3.
- [17] M. Manzoni, S. Tebaldini, A. V. Monti-Guarnieri, and C. M. Prati, "Multipath in automotive MIMO SAR imaging," *IEEE Trans. Geosci. Remote Sens.*, vol. 61, pp. 1–12, 2023.
- [18] Y. Jia et al., "Multipath ghost and side/grating lobe suppression based on stacked generative adversarial nets in MIMO through-wall radar imaging," *IEEE Access*, vol. 7, pp. 143367–143380, 2019.
- [19] R. Feng, E. De Greef, M. Rykunov, H. Sahli, S. Pollin, and A. Bourdoux, "Multipath ghost classification for MIMO radar using deep neural networks," in *Proc. IEEE Radar Conf. (RadarConf22)*, 2022, pp. 1–6.
- [20] P. Wu, J. Chen, S. Guo, G. Cui, L. Kong, and X. Yang, "NLOS positioning for building layout and target based on association and hypothesis method," *IEEE Trans. Geosci. Remote Sens.*, vol. 61, pp. 1–13, 2023.
- [21] J. Chen, S. Guo, H. Luo, N. Li, and G. Cui, "Non-line-of-sight multi-target localization algorithm for driver-assistance radar system," *IEEE Trans. Veh. Technol.*, vol. 72, no. 4, pp. 5332–5337, Apr. 2023.
- [22] S. Buzzi, E. Grossi, M. Lops, and L. Venturino, "Foundations of MIMO radar detection aided by reconfigurable intelligent surfaces," *IEEE Trans. Signal Process.*, vol. 70, pp. 1749–1763, 2022.
- [23] F. Engels, M. Wintermantel, and P. Heidenreich, "Automotive MIMO radar angle estimation in the presence of multipath," in *Proc. Eur. Radar Conf. (EURAD)*, Nuremberg, Piscataway, NJ, USA: IEEE Press, Oct. 2017, pp. 82–85.
- [24] B. Li, S. Wang, J. Zhang, X. Cao, and C. Zhao, "Ultra-fast accurate AoA estimation via automotive massive-MIMO radar," *IEEE Trans. Veh. Technol.*, vol. 71, no. 2, pp. 1172–1186, Feb. 2022.
- [25] X. Zhang, L. Xu, L. Xu, and D. Xu, "Direction of departure (DOD) and direction of arrival (DOA) estimation in MIMO radar with reduced-dimension MUSIC," *IEEE Commun. Lett.*, vol. 14, no. 12, pp. 1161–1163, Dec. 2010.
- [26] H. Jiang, J.-K. Zhang, and K. M. Wong, "Joint DOD and DOA estimation for bistatic MIMO radar in unknown correlated noise," *IEEE Trans. Veh. Technol.*, vol. 64, no. 11, pp. 5113–5125, Nov. 2015.
- [27] H. Luo, Z. Zhu, M. Jiang, S. Guo, and G. Cui, "An effective multipath ghost recognition method for sparse MIMO radar," *IEEE Trans. Geosci. Remote Sens.*, vol. 61, pp. 1–11, 2023.
- [28] Y. Li and X. Shang, "Multipath ghost target identification for automotive MIMO radar," in *Proc. IEEE 96th Veh. Technol. Conf. (VTC2022-Fall)*, London, U.K. Piscataway, NJ, USA: IEEE Press, Sep. 2022, pp. 1–5.
- [29] Z. Zhu et al., "Non-line-of-sight targets localization algorithm via joint estimation of DoD and DoA," *IEEE Trans. Instrum. Meas.*, vol. 72, pp. 1–11, 2023.
- [30] L. Zheng, A. Maleki, H. Weng, X. Wang, and T. Long, "Does ℓ_p -minimization outperform ℓ_1 -minimization?" *IEEE Trans. Inf. Theory*, vol. 63, no. 11, pp. 6896–6935, 2017.
- [31] Q. Xie, X. Pan, M. Huang, J. Chen, and S. Xiao, "Sparsity-based direction-of-departure and direction-of-arrival estimation for bistatic multiple-input multiple-output radar," *IEEE Access*, vol. 7, pp. 118826–118838, 2019.
- [32] T. Strohmer and B. Friedlander, "Analysis of sparse MIMO radar," *Appl. Comput. Harmon. Anal.*, vol. 37, no. 3, pp. 361–388, 2014. [Online]. Available: <https://www.sciencedirect.com/science/article/pii/S1063520314000037>
- [33] B. Jakanovic and M. Amin, "Reduced interference sparse time-frequency distributions for compressed observations," *IEEE Trans. Signal Process.*, vol. 63, no. 24, pp. 6698–6709, Dec. 2015.
- [34] L. Zheng and X. Wang, "Super-resolution delay-Doppler estimation for OFDM passive radar," *IEEE Trans. Signal Process.*, vol. 65, no. 9, pp. 2197–2210, May 2017.
- [35] H. Rohling and M.-M. Meinecke, "Waveform design principles for automotive radar systems," in *Proc. CIE Int. Conf. Radar Proc. (Cat No. 01TH8559)*, 2001, pp. 1–4.
- [36] M. Kronauge and H. Rohling, "New chirp sequence radar waveform," *IEEE Trans. Aerosp. Electron. Syst.*, vol. 50, no. 4, pp. 2870–2877, Oct. 2014.
- [37] K. Doris, A. Filippi, and F. Jansen, "Reframing fast-chirp FMCW transceivers for future automotive radar: The pathway to higher resolution," *IEEE Solid-State Circuits Mag.*, vol. 14, no. 2, pp. 44–55, Spring 2022.
- [38] X. Wang, M. Jia, X. Meng, and T. Zhang, "Multipath ghosts mitigation for radar-based positioning systems," in *Proc. IEEE 96th Veh. Technol. Conf. (VTC2022-Fall)*, London, U.K. Piscataway, NJ, USA: IEEE Press, Sep. 2022, pp. 1–6.
- [39] A. B. Baral and M. Torlak, "Joint Doppler frequency and direction of arrival estimation for TDM MIMO automotive radars," *IEEE J. Sel. Topics Signal Process.*, vol. 15, no. 4, pp. 980–995, Jun. 2021.
- [40] P. Wang, P. Boufounos, H. Mansour, and P. V. Orlik, "Slow-time MIMO-FMCW automotive radar detection with imperfect waveform separation," in *Proc. IEEE Int. Conf. Acoust., Speech Signal Process. (ICASSP)*, 2020, pp. 8634–8638.
- [41] L. L. Scharf and B. Friedlander, "Matched subspace detectors," *IEEE Trans. Signal Process.*, vol. 42, no. 8, pp. 2146–2157, Aug. 1994.
- [42] E. L. Lehmann and J. P. Romano, *Uniformly Most Powerful Tests*. New York, NY, USA: Springer-Verlag, 2005, pp. 56–109.
- [43] Z. Yang and L. Xie, "Exact joint sparse frequency recovery via optimization methods," *IEEE Trans. Signal Process.*, vol. 64, no. 19, pp. 5145–5157, Oct. 2016.
- [44] A. Aich and P. Palanisamy, "On-grid DOA estimation method using orthogonal matching pursuit," in *Proc. Int. Conf. Signal Process. Communication (ICSPC)*, 2017, pp. 483–487.
- [45] H. P. Gavin, "The Levenberg-Marquardt algorithm for nonlinear least squares curve-fitting problems," Dept. Civil Environ. Eng., Duke Univ., vol. 19, 2019.

- [46] W. Roberts, P. Stoica, J. Li, T. Yardibi, and F. A. Sadjadi, "Iterative adaptive approaches to MIMO radar imaging," *IEEE J. Sel. Topics Signal Process.*, vol. 4, no. 1, pp. 5–20, Feb. 2010.
- [47] R. Tibshirani, "Regression shrinkage and selection via the Lasso: A retrospective," *J. Roy. Statist. Soc. Ser. B Statist. Methodol.*, vol. 73, no. 3, pp. 273–282, Apr. 2011.
- [48] S. Boyd, N. Parikh, E. Chu, B. Peleato, and J. Eckstein, "Distributed optimization and statistical learning via the alternating direction method of multipliers," *Found. Trends Mach. Learn.*, vol. 3, no. 1, pp. 1–122, Jan. 2011, doi: 10.1561/22000000016.
- [49] B. Ottersten, M. Viberg, P. Stoica, and A. Nehorai, *Exact and Large Sample Maximum Likelihood Techniques for Parameter Estimation and Detection in Array Processing*. Berlin, Germany: Springer-Verlag, 1993, pp. 99–151.



Le Zheng (Senior Member, IEEE) received the B.Eng. degree from the Northwestern Polytechnical University, Xi'an, China, in 2009, and the Ph.D. degree from Beijing Institute of Technology (BIT), Beijing, China, in 2015. Previously, he has held academic positions with the Electrical Engineering Department, Columbia University, New York, NY, USA, first as a Visiting Researcher, from 2013 to 2014, and then as a Postdoctoral Research Fellow, from 2015 to 2017. From 2018 to 2022, he was with Aptiv, Los Angeles, as a Principal Radar Systems

Engineer, leading projects on the next-generation automotive radar products. Since 2022, he has been a Full Professor with the School of Information and Electronics, BIT. His research interests include general research radar, statistical signal processing, wireless communication, and high-performance hardware, in particular in the area of automotive radar and integrated sensing and communications. He is a Founding Member of the IEEE ComSoc ISAC Emerging Technology Initiative. He is the Guest Editor of IEEE JOURNAL OF SELECTED TOPICS IN SIGNAL PROCESSING Special Issue on Joint Communication and Radar Sensing and *IEEE Wireless Communications* Special Issue on Integrated Sensing and Communications for 6G.



Jiamin Long received the B.S. degree in communication engineering from the Northeastern University, Qinhuangdao, in 2019. She is currently working toward the Eng.D. degree with the Radar Research Laboratory, School of Information and Electronics, Beijing Institute of Technology, Beijing, China. Her research interests include automotive radar, MIMO radar, and signal processing.



Marco Lops (Fellow, IEEE) received the Laurea and Ph.D. degrees from "Federico II" University. He was first an Assistant Professor and then an Associate Professor with the University of Naples Federico II. In 2000, he moved to the University of Cassino and Southern Lazio as a Full Professor and he returned to the University of Naples Federico II in 2018. From 2009 to 2012, he was also with ENSEEIHT, Toulouse, France, first as a Full Professor (on leave of absence from Italy) and then as a Visiting Professor. In 2008, he was a Visiting

Professor with the University of Minnesota and in 2009 Columbia University. Previously, he had also held visiting positions with the University of Connecticut, Rice University, and Princeton University. He is currently a Professor with the Department of Electrical and Information Technology (DIETI), University of Naples Federico II, Italy. He has authored or co-authored more than 90 scientific papers published on refereed journals. His research interests include detection and estimation, with emphasis on communications and radar signal processing. He was a coreipient (with Ezio Biglieri) of the 2014 Best Paper Award from the Journal of Communications and Networks. From 2009 to 2015, he served two terms for the Sensor Array and Multichannel Signal Processing Technical Committee (SAM). He has served as an Associate Editor for *Journal of Communications and Networks*, IEEE TRANSACTIONS ON INFORMATION THEORY (Area: Detection and Estimation, two terms), IEEE SIGNAL PROCESSING LETTERS, and IEEE TRANSACTIONS ON SIGNAL PROCESSING (two terms). He also served as a Senior Area Editor for IEEE TRANSACTIONS ON SIGNAL PROCESSING. He was selected to serve as a Distinguished Lecturer for the Signal Processing Society from 2018 to 2020.



Fan Liu (Senior Member, IEEE) received the B.Eng. and Ph.D. degrees from Beijing Institute of Technology (BIT), Beijing, China, in 2013 and 2018 respectively, respectively. He is currently an Assistant Professor with the School of System Design and Intelligent Manufacturing (SDIM), Southern University of Science and Technology (SUSTech). He has previously held academic positions with the University College London (UCL), first as a Visiting Researcher from 2016 to 2018, and then as a Marie Curie Research Fellow from 2018 to 2020. His

research interests include signal processing and wireless communications, and in particular in the area of Integrated Sensing and Communications (ISAC). He has 10 papers selected as IEEE ComSoc Best Readings. He is the founding Academic Chair of the IEEE ComSoc ISAC Emerging Technology Initiative (ISAC-ETI), an Elected Member of the IEEE SPS Sensor Array and Multichannel Technical Committee (SAM-TC), a Founding Member of the IEEE SPS ISAC Technical Working Group (ISAC-TWG), an Associate Editor of IEEE TRANSACTIONS ON MOBILE COMPUTING, IEEE OPEN JOURNAL OF SIGNAL PROCESSING and IEEE COMMUNICATIONS LETTERS, and a Guest Editor of IEEE JOURNAL ON SELECTED AREAS IN COMMUNICATIONS (JSAC), IEEE WIRELESS COMMUNICATIONS, and *IEEE Vehicular Technology Magazine*. He has served as the organizer and Co-Chair for several workshops, special sessions and tutorials in flagship IEEE conferences, including ICC, GLOBECOM, ICASSP, SPAWC, and MobiCom. He is a TPC Co-Chair of the 2nd–4th IEEE Joint Communication and Sensing (JC&S) Symposium, a Symposium Co-Chair for IEEE GLOBECOM 2023, and a Track Co-Chair for the IEEE WCNC 2024. He is a member of the IMT-2030 (6G) ISAC Task Group. He was listed among the World's Top 2% Scientists by Stanford University for citation impact from 2021 to 2023, and among the 2023 Elsevier Highly-Cited Chinese Researchers. He was the recipient of the 2023 IEEE Communications Society Stephan O. Rice Prize, 2023 IEEE ICC Best Paper Award, 2023 IEEE/CIC ICC 2023 Best Paper Award, 2022 First Prize of Science and Technology Progress of China Institute of Communications, 2021 IEEE Signal Processing Society Young Author Best Paper Award, 2019 Best Ph.D. Thesis Award of Chinese Institute of Electronics, 2018 EU Marie Curie Individual Fellowship, and has been named as an Exemplary Reviewer for IEEE TWC/TCOM/COMML for 5 times.



Xueyao Hu received the B.S. degree in detection guidance and control technology from Nanjing University of Science and Technology, Jiangsu, China, in 2013, and the Ph.D. degree in target detection and recognition from Beijing Institute of Technology, Beijing, China, in 2020, respectively. He is currently an Associate Professor with the School of Information and Electronics, Beijing Institute of Technology, Beijing, China. His research interests include radar signal processing, sparse representation theory, and millimeter-wave radar

system design.



Chuanhao Zhao received the B.S. degree in electronic science and technology from Beijing University of Chemical Technology, in 2022. He is currently working toward the master's degree with the Radar Research Laboratory, School of Information and Electronics, Beijing Institute of Technology, Beijing, China. His research interests include automotive radar and signal processing.